Spring 5-19-2017

Design and Computational Fluid Dynamics Analysis of an Idealized Modern Wingsuit

Maria E. Ferguson
Washington University in St Louis

WASHINGTON UNIVERSITY IN ST. LOUIS
School of Engineering and Applied Science
Department of Mechanical Engineering and Materials Science

Thesis Examination Committee:
Dr. Ramesh Agarwal, Chair
Dr. Qiulin Qu
Dr. David Peters

Design and Computational Fluid Dynamics Analysis of an Idealized Modern Wingsuit

by

Maria E. Ferguson

A thesis presented to the School of Engineering and Applied Science
of Washington University in St. Louis in partial fulfillment
of the requirements for the degree of
Master of Science

May 2017
St. Louis, Missouri

Table of Contents

List of Figures

List of Tables

Acknowledgements

I began this project with an ardent desire to research the aerodynamics of wingsuits—a subject very much lacking in the available literature—and no skills or background in Computational Fluid Dynamics whatsoever. I would like to extend my sincerest thanks to Dr. Ramesh Agarwal for his support of an unconventional topic and his guidance throughout the entire design and analysis process. He supported my passion and continuously gave the project direction, guiding my efforts toward the eventual design and CFD analysis of my own wingsuit. None of my research would have been possible without him, and I have enjoyed myself every step of the way.

A big thank you to Dr. Qiulin Qu, whose input was invaluable to this project. His help with ANSYS Fluent and his aerodynamics insight were key to my progress, and his personal attention to my endeavors provided continuous encouragement to take my research to new heights.

I would also like to thank my fellow CFD lab member, Boshun Gao, for his instructions and assistance with ANSYS software, especially throughout the meshing process. Thanks to Timothy Wray for his help in orienting me in the use of ANSYS and guidance in the early stages of this project. Thanks to Francis Acquaye for constant sanity checks, proof editing, and emotional support.

Finally, I would like to thank both my parents for making my undergraduate and graduate engineering studies possible, and for their unwavering love and support as I pursued my dreams. They are my rock and my inspiration, and I thank them from the bottom of my heart.

Maria E. Ferguson

Washington University in St. Louis

May 2017

For my parents, Nancy and Wendell Ferguson.

ABSTRACT OF THE THESIS

Design and Computational Fluid Dynamics Analysis of an Idealized Modern Wingsuit

by

Maria E. Ferguson

Master of Science in Aerospace Engineering

Washington University in St. Louis, 2017

Research Advisor: Dr. Ramesh Agarwal

The aerodynamics of a modern wingsuit has been the subject of very few detailed scientific studies to date. The prevailing design process remains the dangerous "sew and fly" method, in which designs are tested when they are first flown. This study utilizes Computational Fluid Dynamics (CFD) tools to analyze the flow field and aerodynamics of an idealized wingsuit, which is designed using Computer-Aided Design (CAD) modeling. The 3D CAD software Autodesk Inventor is used to create the wingsuit model, which is designed with a Gottingen 228 airfoil cross-section and a relatively large planform of aspect ratio 1.3. The commercial flow solver ANSYS Fluent is employed to solve the steady Reynolds-Averaged Navier-Stokes (RANS) equations with a turbulence model. First, the CFD simulations were performed using the k-kl-ω Transition turbulence model for flow past the Gottingen 228 airfoil in 2D at various angles of attack. This was done in order to validate the computations against the results from the airfoil software Profili 2.0, ensuring that the CFD solutions matched the lift and drag coefficients obtained from Profili. The airfoil had a maximum lift coefficient of 1.97 and a stall angle of 12°. After the validation, 3D RANS simulations were performed for flow past the wingsuit at various angles of attack using the Spalart-Allmaras turbulence model. The wingsuit was assumed to be flying with a free-stream velocity of 45 m/s, corresponding to a Reynolds number of 5.5×10^6. The 3D wingsuit had a maximum lift coefficient of 2.73 and reached a stall angle of 47°, which are higher than the 2D case because of the effect of induced drag on the 3D wing. The 3D results were proved to be grid independent. The wingsuit was found to be statically stable for 18–23° angles of attack and higher, where the angle of attack indicating the onset of the stable region depended on the physiology of the flyer. The lack of experimental data for wingsuit flight in the literature made the full 3D validation of the CFD results

impossible to achieve. Nevertheless, the results of the 3D wingsuit were thoroughly analyzed and compared to those for rectangular flat plate wings of similar aspect ratio at the same Reynolds number. The results compared well and indicated that the designed wingsuit should perform well aerodynamically under typical wingsuit flying conditions. This study paves the way for practical wingsuit design for commercial use.

Chapter 1 Introduction

1.1 Wingsuit Development and History

1.1.1 Background

The quest toward human flight did not end with the airplane. The desire simply to *fly* does not sufficiently explain that yearning to soar through the skies. That age-old desire is to *fly like birds*, unimpeded by heavy machinery. As Michael Abrams mentions in his history *Birdmen, Batmen, and Skyflyers*, if piloting a plane is flying, then rowing a canoe is swimming [1]. Unlike a hang glider, jet pack, or small plane, the wingsuit avoids excessive apparatus or motors and allows the flyer to glide on his or her own power.

The sport of wingsuit flying adds the element of glide to skydiving and BASE (Building, Antenna, Span, and Earth) jumping. Skydivers and BASE jumpers jump out of planes or off tall objects, go into free fall, and then pull a parachute at a certain altitude above the ground. Wingsuit flyers, on the other hand, wear suits that allow them to glide through the air before they eventually lose altitude and pull their parachutes. The flying squirrel–like suits are made of flexible and durable parachute fabric and have two wings, one below the arms and one between the legs, creating a surface that generates as much lift as possible given the limitations of the human body [2].

The modern wingsuit has only been in existence since the 1990s [3], and although academics and manufacturers have begun to take a more scientific approach to wingsuit design, only a handful of truly rigorous analyses have been conducted thus far. The lack of information on wingsuit aerodynamics puts the designers and flyers at a dangerous disadvantage.

In fact, the quest for human flight has been deadly for the vast majority of would-be birdmen. In the attempt to fashion the first set of viable human wings, the emphasis was never on the aerodynamics of flight, but merely on the dream that if one found the right combination of feathers, fabric, wood, or bone, a plummeting fall would turn into a graceful glide. For centuries, daredevils across the world have died in the attempt to create an apparatus to accomplish this goal.

1.1.2 History

The quest to achieve human flight has a long and rich history with many colorful failures alongside the successes. Ancient myths of human flight appear in countless cultures, including the Greeks,

Chinese, Aztecs, Incas, Hindu, Egyptians, and Norse. Legends of successful flights using cloth or wooden wings abound, from Chinese Emperor Shun flying to escape a tower before 2233 BC to Armen Firman jumping off a city tower in mid-ninth century Cordova, Spain. After the end of the first millennium, documented attempts to jump from stationary heights tell a less successful story, with many tales of men jumping from heights with various apparatus and falling to serious injury or death. Some of these daredevils miraculously managed to fall without breaking bones, or even, supposedly, to glide some distance, but the impact of landing posed a perennial problem for early pioneers [1].

In 1912, Austrian tailor Franz Reichelt attempted the first wingsuit flight of the twentieth century in a hand-sewn "parachute suit." He fell 377 feet from the second platform of the Eiffel Tower, straight to his death. The year of his death coincided with the first parachute jump from an airplane, which heralded in a new era of testing wings from airplanes and using a parachute to land [1].

Figure 1: The "Flying Tailor" Franz Reichelt, 1912 [18]

From 1930 to the early 1960s, 72 of 75 aspiring birdmen died in the attempt. The earliest wingsuit success was achieved by Clem Sohn in 1935, using a rigid frame to create bat-like wings. The most famous early wingsuit was developed—along with modern skydiving technique—by Leo Valentin in the 1940s, with his first successful flight in 1954. Valentin, marketed as "the Bird Man," made huge strides forward in the quest for unassisted human flight. In 1956, however, while testing his large, rigid wings, the air pulled him from the plane prematurely and sent him into a violent spin. He deployed his parachute, but the lines twisted and caught on the wings, and he perished like his predecessors [1].

Prior to settling on a rigid wing, Valentin experimented with canvas wings and deemed them ineffective. However, the rigidity in his wing and Sohn's bat suit made their suits dangerous, since the wood or metal frames could easily interfere with the parachute or be subjected to gusts that

rendered them uncontrollable. The key to creating an effective fabric suit was first developed by Tom Sitton in the 1960s by sewing vented cells in the fabric in imitation of parachutes. The cells would then inflate to create ram-air wings, which for the first time allowed a fabric suit to have thickness, shape, and some amount of rigidity [1].

The modern wingsuit used today was not developed until the 1990s, and was created by a man named Patrick de Gayardon. Using sturdy parachute fabric, he fashioned a flexible wingsuit with two ram-air wings, one under the arms and one between the legs. This allowed him to glide through the air like a bird for about a minute until he lost enough altitude to pull his parachute. Like Valentin before him, he was known as the "bird man" and inspired awe among the skydiving community and the world at large until his tragic death in a skydiving accident [1].

Figure 2: Patrick de Gayardon, 1990s [19]

Since de Gayardon's death, several companies have imitated his wingsuit design and made wingsuits available for public purchase. The first wingsuit company, established in 1999, was named "Birdman" in honor of the 20th century daredevils that had come before [4]. The sport is still small—Robert Pecnik, founder of Phoenix-Fly Design and co-founder of Birdman International, estimated in 2010 that there might be 600 flyers worldwide. About 40 or 50 of these are proximity flyers who BASE jump from cliffs and buildings and fly in close proximity to the ground [5]. This number has almost certainly increased over the past seven years, but wingsuit flyers still constitute a niche group.

Historically, the vast majority of wingsuit development has been completed in the "sew and fly" fashion, where pioneers essentially test their designs using a guess and check method. Unfortunately, many daredevils have guessed wrong. More recently, however, academics and engineers have conducted experiments to inspect the aerodynamics of wingsuit flight, and it is expected that studies like these should once again revolutionize wingsuit flight.

1.1.3 Typical Wingsuit Flying Conditions

According to HowStuffWorks, typical wingsuit horizontal velocity ranges from 31 m/s to 40 m/s, while the vertical velocity ranges from 22 m/s to 27 m/s [2]. In their AIAA-published paper, Rafaello D'Andrea and Geoffrey Robson claim that a comfortable flying speed is 35 m/s, and that the maximum glide ratio can be comfortably obtained at 45 m/s [6].

Since the goal of this study was to examine the performance of an idealized wingsuit under optimal conditions, 45 m/s was chosen as the free-stream velocity. Although some record-breaking wingsuit flights have been attained at higher altitudes (and some daredevils have jumped at lower ones), 10,000 feet is a typical altitude for skydivers to exit the plane, so air properties were obtained at 10,000 feet to calculate the free-stream Reynolds number. There is, of course, variation based on weather and exact location, but the approximation was considered sufficient for the purpose of this study.

1.2 Aerodynamic Theory

1.2.1 Airfoil and Wingsuit Aerodynamics

The critical difference between wingsuit flying and skydiving is that the wingsuit converts most of the vertical velocity into horizontal motion as shown in Table 1.

Table 1: Comparison of Velocity Components for Skydivers and Wingsuit Flyers [2]

Velocity Component	**Skydiver (m/s)**	**Wingsuit Flyer (m/s)**	**Skydiver (mph)**	**Wingsuit Flyer (mph)**
Vertical	54	22 – 27	120	50 – 60
Horizontal	13 – 27	31 – 40	30 – 60	70 – 90

This is possible because the wingsuit creates lift, which counteracts the weight of the flyer. The ability to glide horizontally does not, however, imply freedom to move freely through the air. As the flyer glides, small adjustments to their body position drastically affect their trajectory, making

stability a crucial aspect of wingsuit design. Wingsuits suffer from inefficiency in lateral flight [6]—the high forward velocity impedes the flyer's ability to make sharp turns without sacrificing stability. An ideal wingsuit is stable for as many flying conditions as possible, experiences enough drag to extend flying time but not to slow the flight excessively, and has a high glide ratio, corresponding to a high lift coefficient.

The first step to optimizing lift on a wing is to create an airfoil wing cross-section. The standard nomenclature for airfoils is given in Figure 3. An important element in wing design is camber, the curve in the airfoil shape that allows it to generate lift at zero degrees angle of attack. For symmetric airfoils, the camber line is identical to the chord line.

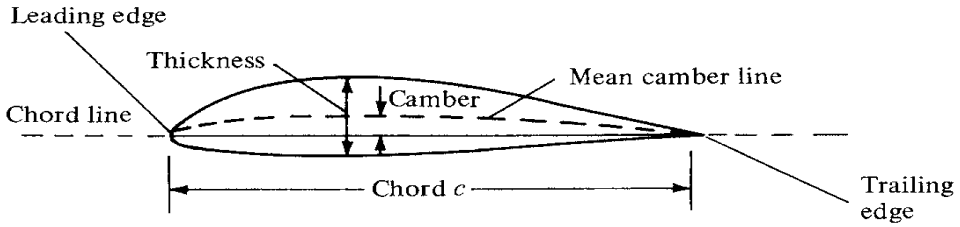

Figure 3: Airfoil nomenclature [9]

Airfoils generate lift; this mechanism can be explained by the relationship between the velocity and the pressure given by the Bernoulli equation for steady frictionless flow [7]:

$$\left(p + \frac{1}{2}\rho V^2\right)_1 = \left(p + \frac{1}{2}\rho V^2\right)_2 \tag{1}$$

The pressure is inversely proportional to the velocity. When a camber or angle of attack is introduced to an airfoil, the velocity on the top surface exceeds that on the lower surface. The higher velocity of the air over the top surface of the airfoil creates lower pressure above the airfoil, while the lower velocity on the underside creates higher pressure below it. This pressure differential creates an upward movement in the flow from the high-pressure region to the low-pressure region, generating lift. The lift on an airfoil increases with angle of attack until stall, at which point the flow detaches and begins to recirculate over the airfoil, sometimes creating a bubble, but always resulting in a loss in lift.

The difficulty, then, is in creating a fabric suit that not only forms a wing, but forms a wing with a high-performance airfoil cross-section. The true genius in de Gayardon's vented fabric suit is the ram-air wings, which uses the incoming airflow to inflate the wings. Wingsuit designers such as Tony Uragallo shape the wingsuit so that the wings actually inflate in the form of an airfoil to generate lift.

While many wingsuits provide glide ratios of 2 vertical units of length for every horizontal unit lost in altitude, the Tony Uragallo design provides an impressive glide ratio of 3.6 to 1. Simply by taking advantage of the airfoil shape, flyers can dive to gain speed and actually swoop upward, gaining altitude [8].

1.2.2 Wing Theory

The wingsuit model in this study was created with an exact airfoil cross-section. The idealized scenario lent itself to a comparison of the 2D results for the chosen airfoil cross-section and the 3D results for the wingsuit geometry, since theoretical analyses already exist to compare a wing and its cross-section. Although there is no experimental data readily available for wingsuits, the airfoil and wing management software Profili 2.0 could be used to generate lift and drag data, which could then be used to validate the 2D airfoil case.

In 2D, the angle of attack of the air coming toward the leading edge of the airfoil is the angle of attack that the airfoil experiences. In wing theory, however, the airfoil cross-sections in the wing experience an induced drag caused by downwash, a phenomenon where a small velocity component pushes downward on the wing top surface [9]. This leads to an induced angle of attack, which must be subtracted from the geometric angle of attack to obtain the effective angle of attack (the term "angle of attack" in the following text and plots shall indicate the geometric angle of attack unless otherwise specified). To obtain a general idea of how the effective angle of attack compares to the angle of attack set in the boundary condition, the effective angle of attack can be calculated using

$$\alpha_{eff} = \alpha - \alpha_i \tag{2}$$

[9], where α is the geometric angle of attack and α_i is the induced angle of attack. The induced angle of attack is easily calculated by assuming an elliptic wing. This is a big assumption, but if the motivation is to observe a trend rather than obtain exact values, it is sufficient as an approximation. The following equation from [9] may be used to find α_i,

$$\alpha_i = \frac{C_L}{\pi AR} \tag{3}$$

where C_L is the lift coefficient and AR is the wing aspect ratio. When the plot of lift coefficient vs. angle of attack of a 2D airfoil is compared to that of a 3D wing, it is expected that the 3D curve will

reach a higher angle of attack before stall and have a somewhat similar slope, according to the relation given in [9]:

$$\frac{dC_L}{d\alpha} = a = \frac{a_0}{1+\frac{a_0}{\pi AR(1+\tau)}} \tag{4}$$

where a is the 3D wing slope and a_0 is the slope of its 2D cross-section. The value of τ varies for a general wing planform and τ = 0 for an elliptic wing.

1.2.3 Aircraft Stability

The aerodynamic center of a body is defined as the point about which the aerodynamically generated moment is independent of the angle of attack [9]. In the case of CFD analysis, the moment about the quarter chord can be calculated along with other aerodynamic force coefficients.

Ideally, the aerodynamic center of an aircraft should always be behind its center of gravity. As the angle of attack increases, lift, drag, and moment increase—except that at the aerodynamic center, the moment is constant per the definition of the aerodynamic center. Lift produces a nose-down movement acting at the center of gravity. If the aerodynamic center of the body is in front of the center of gravity, the pitching moment is in the same direction as the nose-down movement and encourages the falling motion. If the aerodynamic center of the body is behind the center of gravity, the pitching moment opposes the nose-down movement and helps to stabilize the aircraft.

Based on the assumption that the moment coefficient is constant at the aerodynamic center and extrapolating from the geometry, we find that given two sets of data, A and B, at different angles of attack,

$$\begin{aligned}(C_M)_A + (C_L)_A\left(\bar{x}_{AC} - \frac{1}{4}\right)(\cos\alpha_A) + (C_D)_A\left(\bar{x}_{AC} - \frac{1}{4}\right)(\sin\alpha_A) \\ = (C_M)_B + (C_L)_B\left(\bar{x}_{AC} - \frac{1}{4}\right)(\cos\alpha_B) + (C_D)_B\left(\bar{x}_{AC} - \frac{1}{4}\right)(\sin\alpha_B)\end{aligned} \tag{5}$$

where $\bar{x}_{AC}$ is the ratio of the aerodynamic center location to the overall height, α is the angle of attack, and the aerodynamic force coefficients C_M, C_L, and C_D for two different angles of attack can be obtained from numerical data points. Given the numerical data, the equation can be solved for $\bar{x}_{AC}$ in order to find the location of the aerodynamic center. The location of the aerodynamic center

varies with angle of attack and its location values can be compared to the constant center of gravity in order to determine the angles of attack for which an aircraft is statically stable.

If the angle is assumed to be small, Equation (5) simplifies to

$$(C_M)_A + (C_L)_A \left(\bar{x}_{AC} - \frac{1}{4}\right) = (C_M)_B + (C_L)_B \left(\bar{x}_{AC} - \frac{1}{4}\right) \tag{6}$$

1.3 Review of Literature

The first commercial wingsuit for public use was not created until 1999, a mere 18 years ago [4]. Despite the long history preceding the flexible ram-air suit, the sport of wingsuit flying is still in its infancy. The articles providing information of any kind on wingsuits number in the dozens, and there is only a handful of publicly available articles that perform aerodynamic analyses with academic rigor.

Information about typical flying conditions can be found on websites and publications such as HowStuffWorks [2], Popular Science [3], and Air & Space Smithsonian [5]. Some wingsuit manufacturing companies, such as Birdman International [4] have information on their websites, and others, such as Tony Suits, publish information on YouTube [8].

In his 2012 thesis, Nyberg discusses the use of Computational Fluid Dynamics (CFD) tools to analyze the Apache Wingsuit, obtaining results for moments and forces at various angles of attack. He found an angle of stall of 40° and no significant unstable behavior for his symmetric and asymmetric wingsuit models, except for an excessive head-down pitching moment that might have been due to his model and not due to the actual wingsuit [10].

In their MIT-based study in 2010, Berry, Las Fargeas, and Blair proposed the addition of a forward wing above the head of the wingsuit flyer and tested their design using a mannequin in a wind tunnel. They found a decrease in the lift-to-drag ratio due to increased lift but higher increased drag. The wingsuit improved lift generation by 15–20%, but increased drag by 55–60%, which resulted in a longer fall time, but shorter flight range [11].

A group of fourth-year students at the University of Southampton proposed to develop the first "scientifically engineered wingsuit" to break the world records for greatest distance, highest altitude, and highest speed in 2016. The Icarus Project was supervised by Dr. Angelo Grubiŝic, a lecturer in Astronautics and Advanced Propulsion and the pilot of the Icarus wingsuit. The complete geometry

of a wingsuit was captured using a laser scanner to create a model, which was then evaluated using CFD to show the pressure distribution on the surface of the suit. The wingsuit was tested using a free-flight test rig in the University of Ontario Climatic Wind Tunnel to replicate the cold temperature at high altitudes and to examine the effects of oxygen deprivation on the pilot. The design was altered to increase the lift-to-drag ratio based upon the CFD and wind tunnel results. Finally, the Icarus team designed an aerodynamic helmet called the "Athena" which was designed to improve the aerodynamics of the pilot in flight [12].

In 2012, Geoffrey Robson and Raffaello D'Andrea performed a longitudinal stability analysis of a jet-powered wingsuit. Unique among other available literature, they obtained actual wingsuit flight data upon which to base their analysis. They obtained a glide equation for wingsuits, using the flight data to calculate the parameters, as well as a thrust requirement for sustained level flight. They examined a thrust configuration in which gas turbine engines were secured to the feet of the flyer, and determined that phugoid mode instability was the primary source of instability. To improve stability, they proposed a computerized vectored thrust method [6].

In 2012, Shields and Mohseni performed a wind tunnel study on the effects of sideslip on the aerodynamics of low aspect ratio, low Reynolds number wings. They cited Torres and Mueller [13] as their primary source for low aspect ratio, low Reynolds number wings and reproduced their study along with additional configurations. Shields and Mohseni's study included rectangular, flat plate wings of aspect ratio 1 and 1.5 at Reynolds numbers of the order of 10^5, similar to this study's wingsuit of aspect ratio 1.3 at a Reynolds number of the order of 10^6. Their wind tunnel results included surface tuft visualizations, experimental values for the aerodynamic loads on the plates, and a thorough analysis explaining the aerodynamic flow patterns [14].

Finally, Michael Abrams' 2006 book provides an excellent non-technical history of wingsuits and their development from ancient times through the modern day [1].

Chapter 2 Wingsuit Design

2.1 Geometry

The first step in creating a computer simulation of a wingsuit in flight is to generate the geometry of the wingsuit. Due in part to issues of intellectual property, along with the flexible nature of the wingsuit, it is difficult to generate a geometry that exactly matches a commercial wingsuit. Additionally, computational limitations require that for the present, the wingsuit must be assumed rigid. The project was therefore approached in an idealized fashion: at a certain instant in time, the wingsuit has a certain shape, and the rigid geometry reflects that shape at that moment. Furthermore, the ideal cross-section for a wingsuit is an airfoil, so although the contours of the human body and the flexible fabric make that ideal unattainable, the cross-section was assumed to be an airfoil.

The geometry was designed as an idealized approximation of the typical planform and cross-section of suits currently on the market. The human body, including head, hands, feet, and body contours, was excluded from the geometry, as was the parachute pack that typically rests like a backpack over the flyer's back.

Typically, the wingspan of a human person is approximately the same as their standing height. The wingspan and height of the suit were designed to be 1.8 m so that the suit could accommodate the body of a tall human.

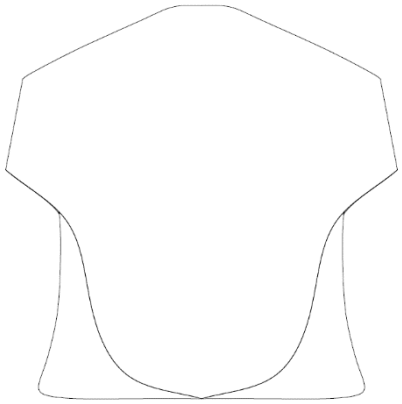

Figure 4: Wingsuit Planform

Some suits, such as Patrick de Gayardon's in Figure 2, have a small forward wing on the arms and a second wing between the legs. Others stretch the fabric such that the forward wing reaches all the way to the legs to create a higher aspect ratio, as shown in Figure 4. The planform for this study was created in imitation of the relatively large aspect ratio suit designed for more experienced flyers. The aspect ratio of the final geometry was 1.3.

After comparing a library of airfoils to images of wingsuits in flight, the Gottingen 228 (GOE 228) airfoil was chosen as the wingsuit cross-section. The GOE 228 was chosen in part for its thickness, since a realistic approximation would have to accommodate the thickness of the human body. It was

also selected for its high camber, along with its lack of a large cavity in the undercamber. Finally, it was chosen for its high lift coefficient due to the camber.

To better understand the rationale behind choosing the GOE 228 airfoil, the popular NACA 0012 airfoil is compared to it in the airfoil and wing management software Profili 2.0.

The important values for the two airfoils are summarized in Table 2. These values demonstrate that the GOE 228 airfoil is a thick airfoil with a large camber and very high lift coefficient.

Table 2: Comparison of GOE 228 and NACA 0012 Airfoils using Profili 2.0 at Re = 2.5×10⁵

Airfoil	**GOE 228**	**NACA 0012**
Max thickness	17.8%	12.0%
Max camber	7%	0%
Stall angle	13.0°	12.5°
Max lift coefficient	1.86	1.06

The geometry and aerodynamic force coefficients of the two airfoils are shown in Figure 5.

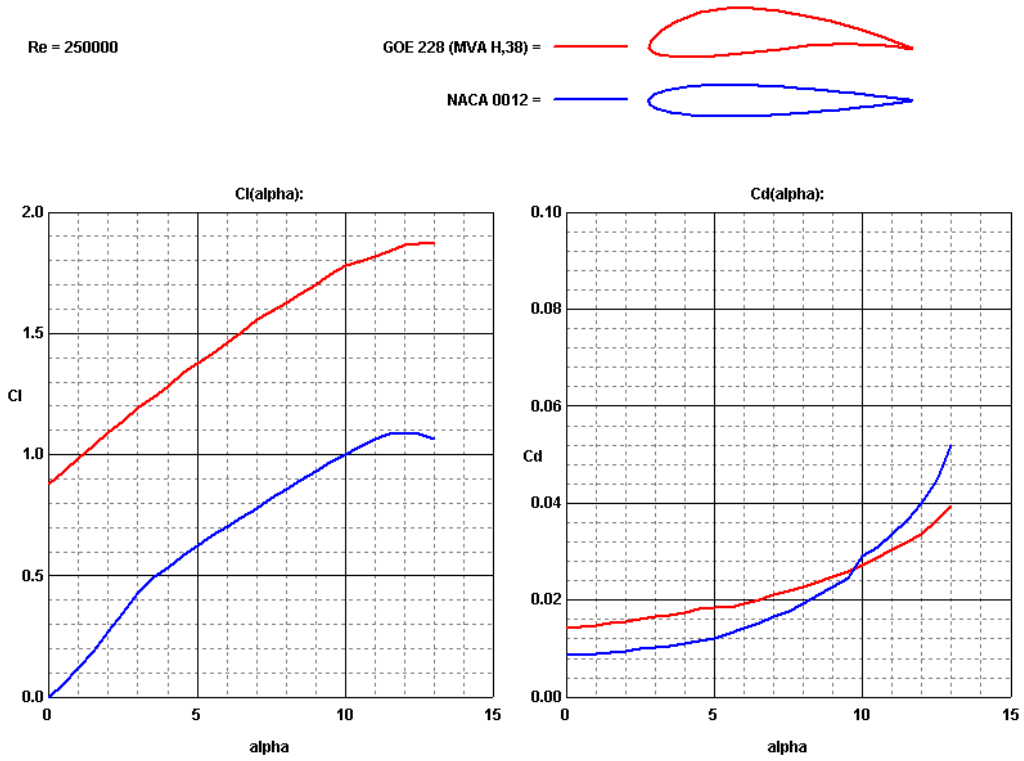

Figure 5: Geometry and aerodynamic force coefficients for the GOE 228 and NACA 0012 airfoils at Re = 2.5×10⁵

2.2 Computer-Aided Design Methodology

The 3D geometry was created with Autodesk Inventor by utilizing the "loft" feature along the line of the planform to connect a center airfoil cross-section to a smaller airfoil cross-section on the wing edge. The resulting wingsuit had an airfoil cross-section at any vertical section cut, except for the very outer edges, where the airfoil cross-section was parallel to the angled wing edge. The edges on the lower half of the suit, near the legs, were unrealistically thin due to the constraints of the CAD software within the available timeframe. The thin areas are visible as the triangular portions on the lower left and right in Figure 4.

Chapter 3 Computational Fluid Dynamics Simulation and Validation

3.1 Computational Fluid Dynamics Background

After the geometry was created, it was imported into the ANSYS ICEM software for meshing. A mesh or grid is the means by which the user specifies the locations around the geometry at which to solve the flow equations—it would be computationally impossible to determine how every particle of air behaves inside the computational domain. The mesh should be denser near the geometry, in its wake, and in any other regions where there are large flow gradients. One value of note is the y+, which is an indication of the mesh quality near the wall, where viscous effects are present—an area that is particularly difficult to solve accurately. The y+ value required for accurate results depends on the specific turbulence model used, but is most important for skin friction and drag calculations, which played a minimal part in this study. Far away from the geometry, the mesh can be less dense to save on computational power. Once the mesh is complete and has been checked for errors, the meshed geometry is transported to the flow solver.

The fundamental equations of viscous fluid flow "have been known for more than 100 years" [7]. The equations are very difficult to solve analytically for all but the simplest problems, and in more complex cases, cannot be solved, even by modern computers. The equations are derived from three conservation laws: conservation of mass, conservation of momentum, and conservation of energy. From the conservation of momentum are derived the Navier-Stokes equations, given in compact vector form below, which are the fundamental equations of viscous fluid flow [7].

$$\rho \frac{D\boldsymbol{V}}{Dt} = \rho \boldsymbol{g} - \boldsymbol{\nabla} p + \frac{\partial}{\partial x_j}\left[\mu\left(\frac{\partial u_i}{\partial x_j} + \frac{\partial u_j}{\partial x_i}\right) + \delta_{ij}\lambda div \boldsymbol{V}\right] \tag{7}$$

For turbulent flow applications, the Navier-Stokes equations can be converted to the Reynolds-Averaged Navier-Stokes (RANS) equations, which are time-averaged. The variables in the instantaneous Navier-Stokes equations (7) above are transformed into mean (time-averaged or ensemble averaged) and fluctuating components in the form $\phi = \bar{\phi} + \phi'$ for scalars, where $\bar{\phi}$ is the mean and ϕ' is the fluctuating component. For the vector quantity velocity, the velocity components are denoted by $u_i = \overline{u_i} + u_i'$ (i = 1, 2, 3). When these expressions are substituted into the

instantaneous Navier-Stokes equations and averaged over time, the RANS equations are obtained [15]:

$$\frac{\partial \rho}{\partial t} + \frac{\partial}{\partial x_i}(\rho u_i) = 0 \tag{8}$$

$$\frac{\partial}{\partial t}(\rho u_i) + \frac{\partial}{\partial x_j}(\rho u_i u_j) = -\frac{\partial p}{\partial x_i} + \frac{\partial}{\partial x_j}\left[\mu\left(\frac{\partial u_i}{\partial x_j} + \frac{\partial u_j}{\partial x_i}\right) - \frac{2}{3}\,\delta_{ij}\frac{\partial u_l}{\partial x_l}\right] + \frac{\partial}{\partial x_j}(-\rho\overline{u_i' u_j'}) \tag{9}$$

It can be seen by comparing Equation (9) and Equation (7) that the RANS equations have a similar form to the instantaneous equations, except that the velocities, pressures, and other solution variables are now time-averaged. The Reynolds stress term $-\rho\overline{u_i' u_j'}$ represents the effects of turbulence, and must be modeled in order to solve Equation (9) [15]. There are a wide variety of turbulence models available in CFD, ranging from single-equation models to more complex models with multiple equations and with various switching functions to change the model behavior in different parts of the flow, such as near a wall or in the wake or shear layers.

3.1.1 Spalart-Allmaras Turbulence Model

The Spalart-Allmaras turbulence model, or S-A model, is a popular one-equation model that "solves a modeled transport equation for the kinematic eddy (turbulent) viscosity" [15]. The S-A model was designed for aerospace applications involving wall-bounded flows and deals well with adverse pressure gradients.

Originally, the S-A model was optimal for low Reynolds numbers only, and required the boundary layer near the wall to be properly resolved, corresponding to a y+ of ~1. ANSYS Fluent has improved the model with an Enhanced Wall Treatment, which removes the y+ sensitivity and allows for $1 < y+ < 30$ [15].

The S-A model is intended for aerodynamic flows, and does not perform well for many industrial flows with recirculation or some free shear flows, especially plane and round jet flows [15].

3.1.2 k-kl-ω Transition Turbulence Model

The S-A model was chosen for its simplicity and efficiency, but when applied to the 2D airfoil validation case, the solution consistently diverged. The k-kl-ω model was then used for the 2D case instead of the S-A model, with excellent results.

The k-kl-ω Transition turbulence model "is used to predict boundary layer development and calculate transition onset" [15]. It is supposed to predict laminar-to-turbulent boundary layer transition. It is a three-equation eddy-viscosity type model, which includes transport equations for turbulent and laminar kinetic energy and the inverse turbulent time scale [15].

3.1.3 Application to Wingsuit

Though there is much to admire in the lives and deaths of those daring individuals who paved the path toward the modern-day wingsuit, we have progressed beyond the "sew and fly" stage. Modern engineering tools provide a means to evaluate the performance and stability of a given wingsuit design before creating it. Computational Fluid Dynamics (CFD) is a particularly useful tool since it allows the designer to test the design, change it, and optimize it before sewing the suit and flying it.

Once a turbulence model has been chosen and employed to calculate the solution of the RANS equations for a given problem, CFD provides numerical results that can be analyzed in useful plots or even visualized on the geometry itself. Figure 6 provides an example of the capabilities of CFD software to visualize the flow about a wingsuit.

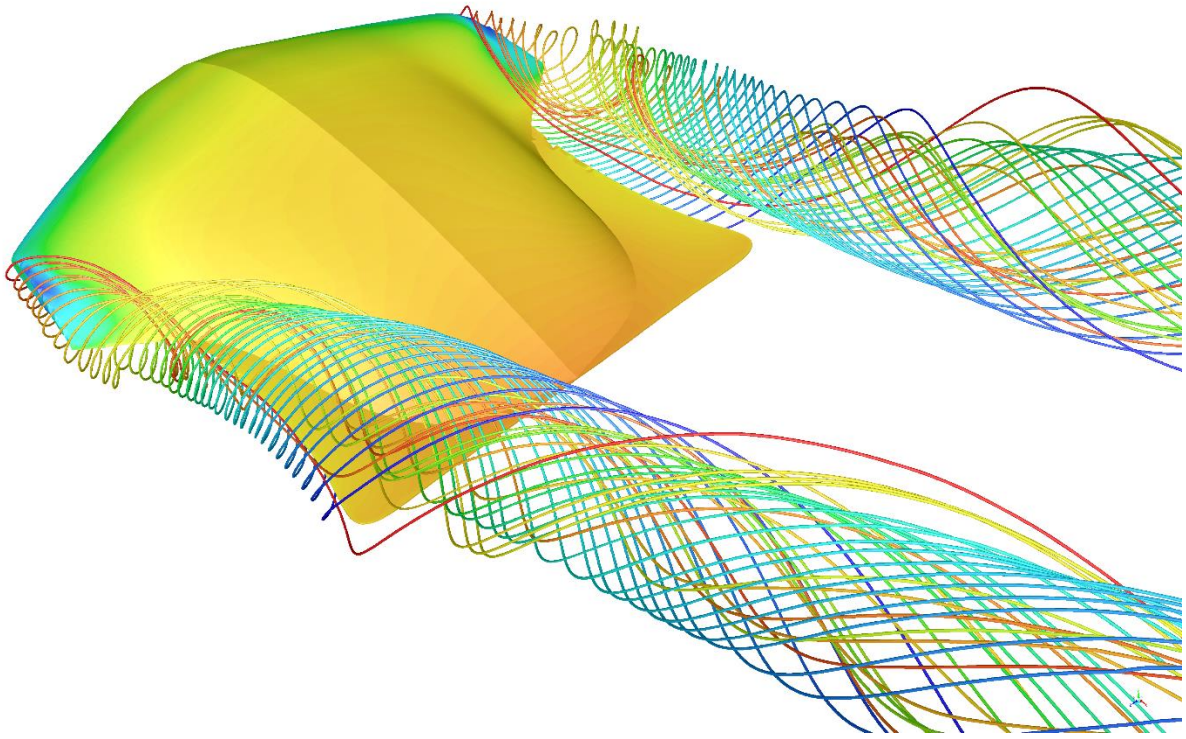

Figure 6: 3D wingsuit at 45 m/s and 32° angle of attack with surface pressure contours and velocity streamlines from wing edges

The pressure contours on the wingsuit are visible as well as the velocity streamlines coming from the wing tips. The leading edge and front wingtips show lower pressure zones, and there is higher pressure on the back side of the wingsuit. The streamlines demonstrate the vortices typical at the tip of a wing.

3.1.4 CFD Limitations

Despite the fact that CFD is a powerful tool, it must be noted that any numerical solution is an approximation. Turbulence is an extremely complex phenomenon that is still beyond the reach of modern computing power to solve from first principles. For this reason, it is a standard practice to validate any CFD solution with experimental data to ensure that the CFD simulation is properly calculating the flow field.

Few scientists have gathered flight data on wingsuits to date, and those who have experimental data have not made it publicly available for CFD validation. In this study, several indirect validation methods are employed to compensate for the lack of experimental data.

3.2 Mesh Generation in ANSYS ICEM

3.2.1 2D Mesh Generation

The 2D mesh for the GOE 228 airfoil was created in the ANSYS meshing software ICEM using a C-topology with a 25 m far field and an airfoil chord length of 1 m, as shown in Figure 7.

The final mesh after refinement had approximately 100,000 elements, with a finer grid near the airfoil and in its wake and with an average y+ value of about 0.47. A more detailed view of the geometry near the airfoil is shown in Figure 8.

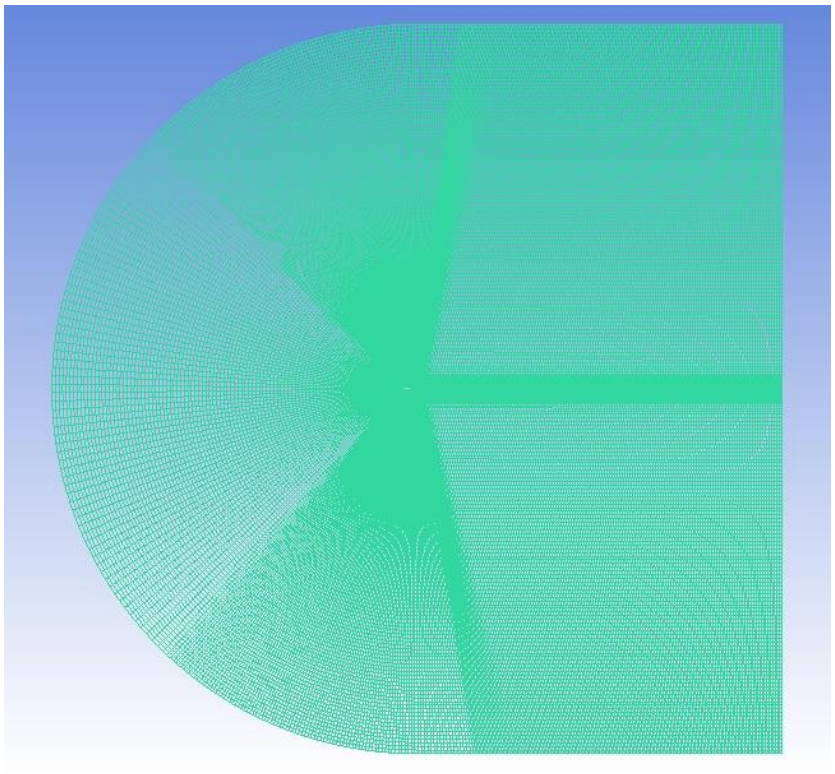

Figure 7: C-topology around the GOE 228 airfoil with 25 m far field

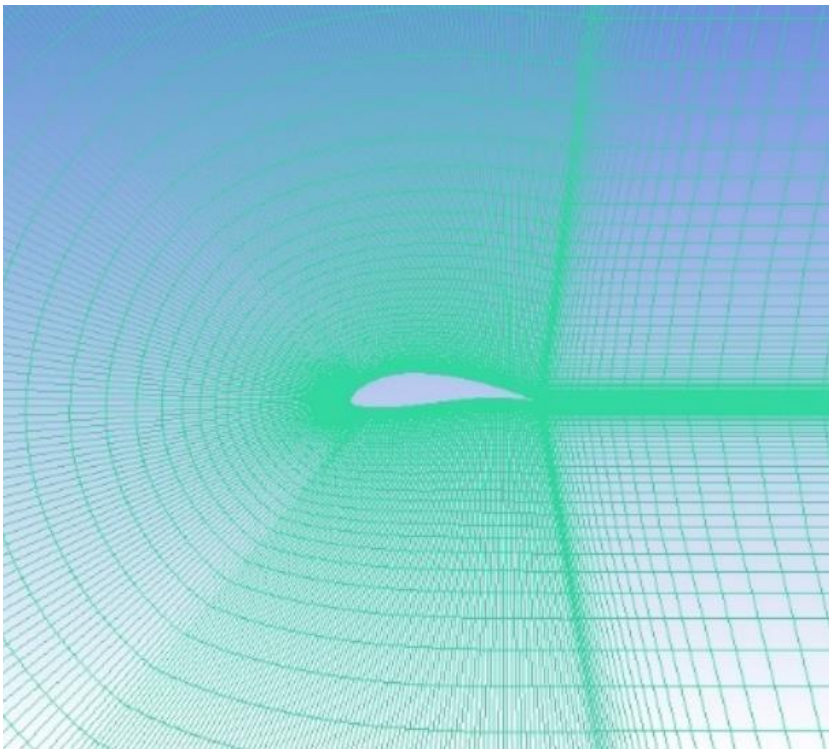

Figure 8: C-topology near the GOE 228 airfoil

3.2.2 3D Mesh Generation

The 3D mesh was also created in ICEM and had a far field in the shape of an elliptical spheroid with major axis 60 m, minor axis 30 m, width 12 m, and a symmetry plane that cut through the middle of the wingsuit geometry. An unstructured mesh was used with prisms near the wingsuit geometry. A dense mesh region at the center was also created to achieve finer resolution close to the geometry. The final mesh had approximately 2.4 million elements and an average wall distance, y+, of 1.43 and is shown in Figure 9.

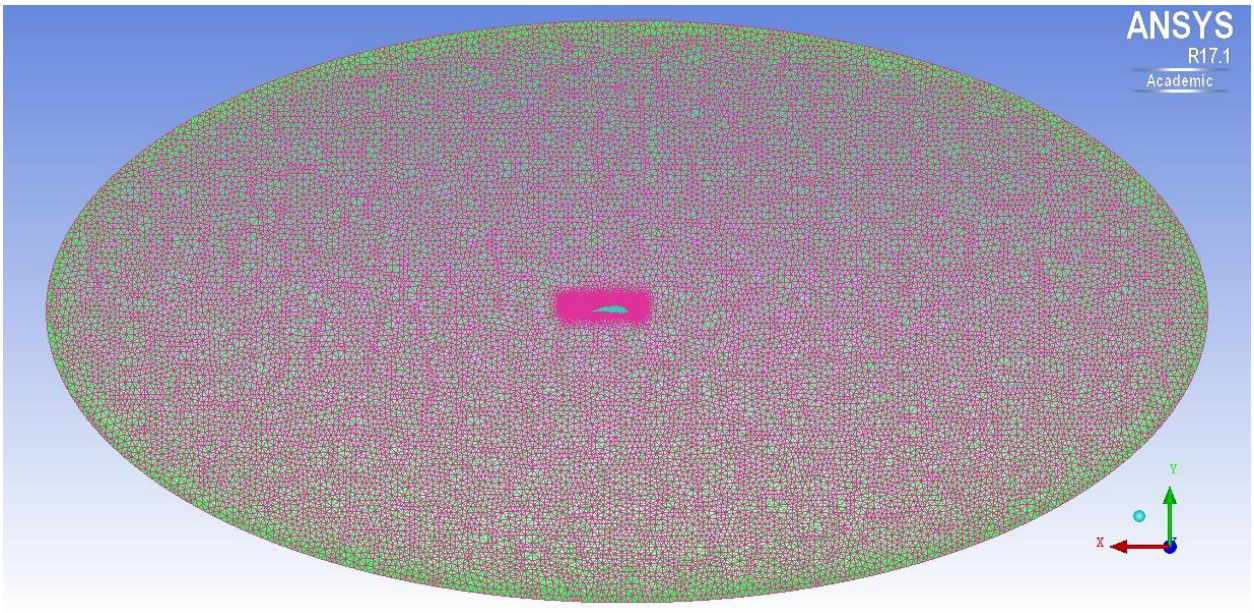

Figure 9: 2.4 million element wingsuit mesh

Since there is no experimental data or simulation results for the wingsuit, it is of vital importance to prove the grid is independent of the computed solution—i.e., to show that the numerical results are not dependent on the mesh and that a finer mesh would yield virtually the same results as the relatively coarse mesh. The finer mesh for the wingsuit was generated with a smaller global element size and containing three mesh density regions with increasing density toward the wingsuit geometry. The finer mesh had approximately 7.4 million elements and is shown in Figure 10.

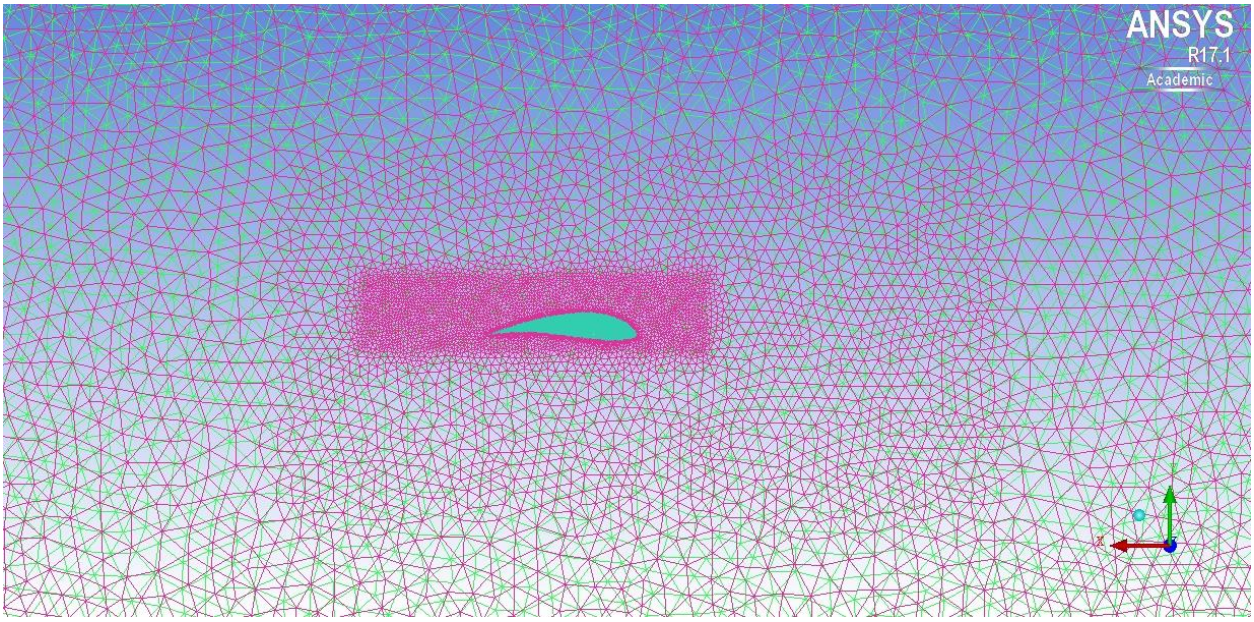

Figure 10: 7.4 million element wingsuit mesh with three mesh density regions

The transition from Autodesk Inventor to ANSYS ICEM and the creation of the symmetry plane created a seam along the middle of the wingsuit because, unfortunately, the cut was not in the exact center of the wingsuit. The error was not discovered until the CFD cases had already been run, so the slight difference between the intended geometry and the resulting geometry was allowed to remain. The seam along the symmetry plane is best viewed in Figure 6.

3.3 Numerical Setup in ANSYS Fluent

3.3.1 2D Airfoil Case

The 2D airfoil case was run in ANSYS Fluent using a pressure-based, viscous, incompressible solver and the k-kl-ω Transition turbulence model with constant air density. The entire geometry was scaled down by a factor of 0.1 to reduce the chord length from 1 m to 0.1 m and to reduce the Reynolds number to 2.4×10^5, a value that could be compared to values in Profili 2.0. The semi-circle in front of the leading edge of the airfoil in Figure 7 was considered a velocity inlet with a magnitude of 45 m/s, which is a reasonable value for a wingsuit in mid-flight and provides the best glide ratio at a comfortable speed [6]. The downstream vertical line was considered a pressure outlet.

The SIMPLE solution scheme with Second Order Upwind discretization was employed. The simulations were run for angles of attack from 0 to 14° in steps of two degrees until the lift and drag coefficients for each case oscillated by less than one percent.

3.3.2 3D Wingsuit Case

The 3D wingsuit case was also run using a pressure-based, viscous, incompressible solver, but with the Spalart-Allmaras turbulence model and air density set to ideal gas. The plane cutting the geometry in half was set as a symmetry plane, and the far field was set as a pressure far field. The Mach number was set at 0.132, which corresponds to a velocity of 45 m/s. The resulting Reynolds number was approximately 3.5×10^6. The area was set to 1 m^2, which would produce nondimensionalized lift and drag coefficients that would later be multiplied by the wingsuit planform half area of 1.25 m^2 to obtain the actual values for the lift and drag coefficients. The length was set to 1.84 m due to a slight measurement error (the actual length was 1.81 m). The momentum coefficient was calculated about the quarter chord at 0.46 m along the x-direction.

The SIMPLE solution scheme with Second Order Upwind discretization was used for the 3D case. The case was run for angles of attack from 0 to 50° in steps of two degrees until 44°, at which point it was run in steps of one degree, until the lift and drag coefficients for each case oscillated by less than one percent.

Chapter 4 2D Airfoil Validation Results

The Reynolds number for the 2D case was 2.4×10^5 assuming the air properties at 3048 m (10,000 feet) and a chord length of 10 cm. The software Profili 2.0 provides airfoil data up to the angle of stall, and this data was compared to the data obtained from Fluent using the k-kl-ω model as shown in Figure 11 and Figure 12. The largest error was at 0° angle of attack, with the Fluent data being 19% and 45% lower than the Profili data for lift and drag coefficient, respectively. Otherwise, the data matched quite well and showed a maximum lift coefficient of 1.97 and a stall angle after 12° angle of attack, as predicted by Profili. The success of this 2D validation case provides greater confidence in the simulation of the 3D wingsuit.

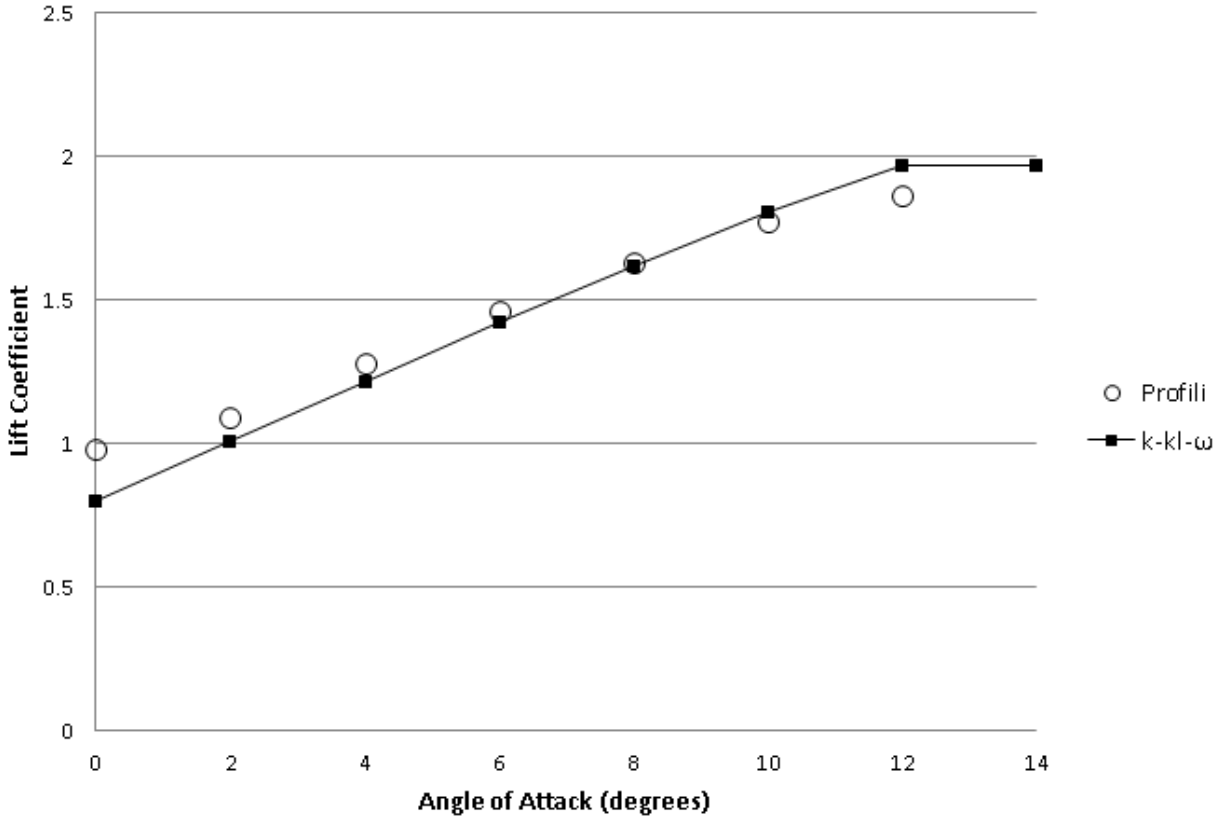

Figure 11: Lift Coefficient values from Profili and CFD results using the k-kl-ω Transition turbulence model

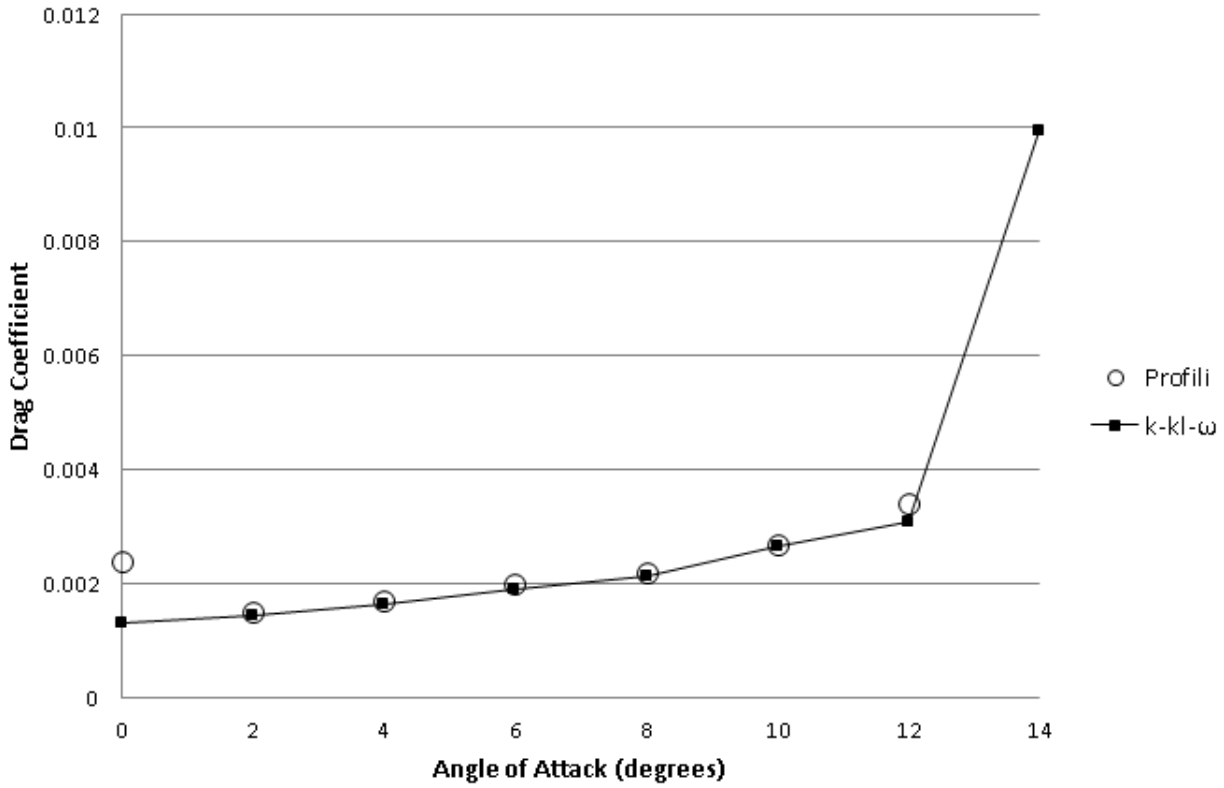

Figure 12: Drag Coefficient values from Profili and CFD results using the k-kl-ω Transition turbulence model

Chapter 5 3D Wingsuit Results

5.1 Aerodynamic Force Coefficients

The 3D computational cases converged within several thousand iterations until about 26° angle of attack, after which point the convergence history showed some oscillations. By 46° angle of attack, the cases were run for tens of thousands of iterations, but eventually the oscillations became small enough to consider the solution converged. The lift increased linearly until 47° angle of attack, at which point a drop in lift appeared. Thus, 47° was considered the stall angle for the wingsuit. An even larger drop in lift coefficient was evident at 48°. The coefficients of lift, drag, and momentum were multiplied by the wingsuit area to obtain the results shown in Figure 13, with a maximum lift coefficient of 2.73. The analysis of the shape of these curves was aided by the insight provided by Shields and Mohseni in their paper "Effects of Sideslip on the Aerodynamics of Low-Aspect-Ratio Low-Reynolds-Number Wings" [14].

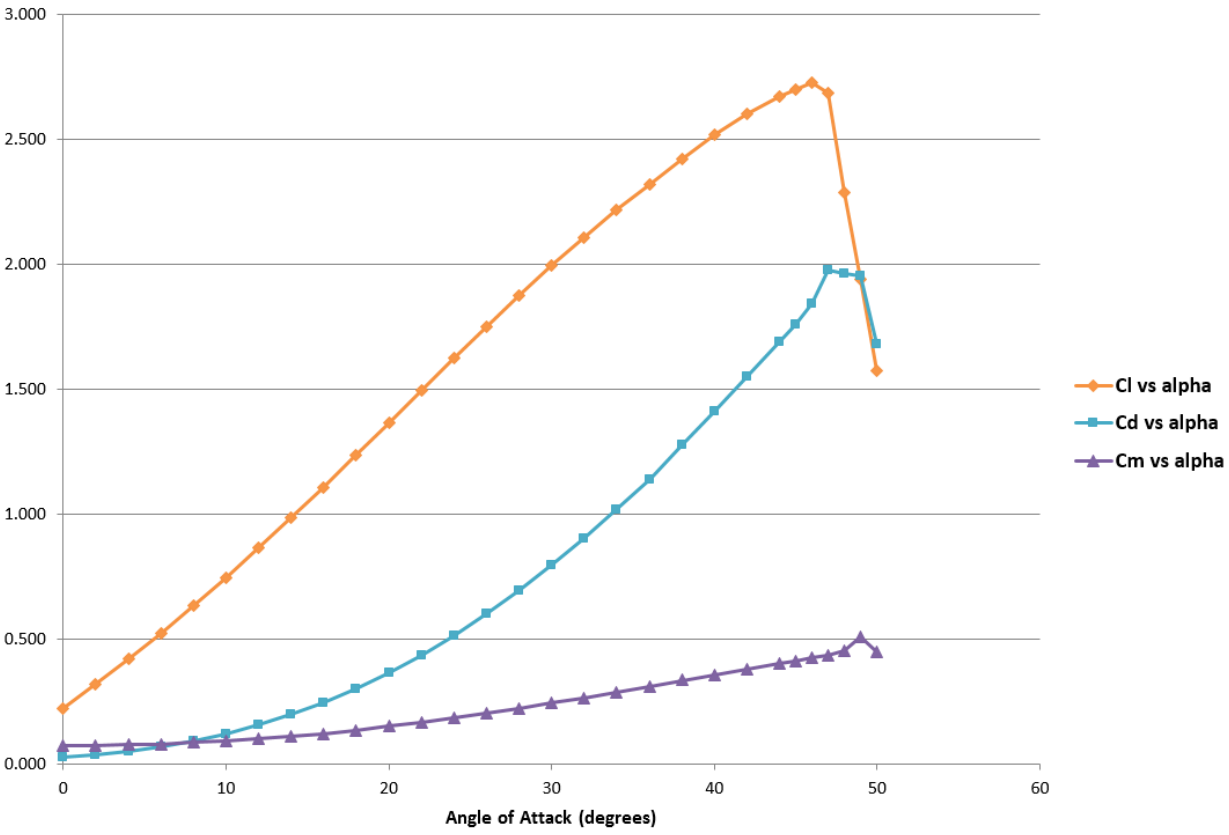

Figure 13: Coefficients of lift, drag, and momentum vs. angle of attack for the 3D wingsuit

The focus of this study was primarily upon the results for the lift coefficient. The general trends in the drag and momentum coefficients were analyzed and used for stability analysis, but the precise numerical results are less useful, because the Spalart-Allmaras turbulence model is most accurate for lift calculations only.

Shields and Mohseni's comments on the unique aerodynamics of low aspect ratio (LAR), low Reynolds number wings also provide insight into the behavior of the flow around the wingsuit. The computed wingsuit lift coefficient and stall angle exceeded expectations. Shields and Mohseni found that a LAR wing actually experiences "an increase in α_{stall} and $C_{L_{max}}$due to the nonlinear lift induced by the interacting flow on the upper wing surface" [14]. They explain that on LAR wings with special airfoil geometries in particular, a separation bubble typically forms on the top surface of the wing due to the strong adverse pressure gradient (a phenomenon that is visible in Figure 27 of this study). They go on to explain that the tip vortex can actually work to increase lift on a LAR wing by generating downwash that forces the vortex sheet to remain attached to the wing surface [14].

Thus, Shields and Mohseni's paper explains, at least in part, the high lift coefficient and stall angle obtained in this study. It also provides a reason for the decrease in linearity in the lift curve in Figure 13 at higher angles of attack: "a decreased AR allows the crossflow produced by the tip vortices to propagate further along the wing and create a nonlinear increase in lift at high angles of attack" [14].

The drop in the drag visible in Figure 13 is also a product of the LAR nature of the wingsuit. It is generally expected that drag will simply increase with angle of attack. However, Shields and Mohseni state that "the detachment of the tip vortices after stall leads to a sudden decrease in drag coefficient as the magnitude of the induced drag drops significantly" [14]. The induced drag has a more powerful effect on the wingsuit or any LAR wing because the effect of downwash is more pronounced.

5.2 Mesh Independence Test

The quality of the computed results was evaluated in three ways: testing for the mesh independence, comparing the 3D wingsuit curves to the 2D airfoil curves, and comparing the 3D wingsuit curves to those for a rectangular flat plate with similar aspect ratio. For the mesh independence test,

computations were performed with a 7.4 million element mesh and a 2.4 million element mesh at 6° and 12° angles of attack, and produced nearly the same results for C_D, C_L, and C_M with less than 1% error, attesting that the results were independent of the mesh. The results of the mesh independence test are given in Table 3.

Table 3: Mesh Independence Test

Mesh elements	**α**	C_L	C_D	C_M
2.4 million	6°	0.526	0.072	0.082
	12°	0.865	0.158	0.103
7.4 million	6°	0.530	0.072	0.083
	12°	0.874	0.160	0.103
% Difference	6°	0.9%	0.8%	0.4%
	12°	0.9%	0.9%	0.5%

5.3 Comparison of 2D and 3D Results Using Wing Theory

When the 3D lift curve was compared to the 2D lift curve, it was found that the 3D wingsuit stalled at an angle of attack of 47°, whereas the 2D airfoil stalled at an angle of attack of 12°. The slope of the 3D curve was also lower than expected based on Equation (4). Based on an airfoil slope of 0.0987, the expected elliptic wing slope would be 0.0975. Although the value of τ for the geometry of the wingsuit is unknown, τ usually ranges from 0.05 to 0.25, which gives the potential predicted wing slope a range of 0.0972 to 0.0975. The slope obtained from CFD was 0.0577, as shown in Figure 14.

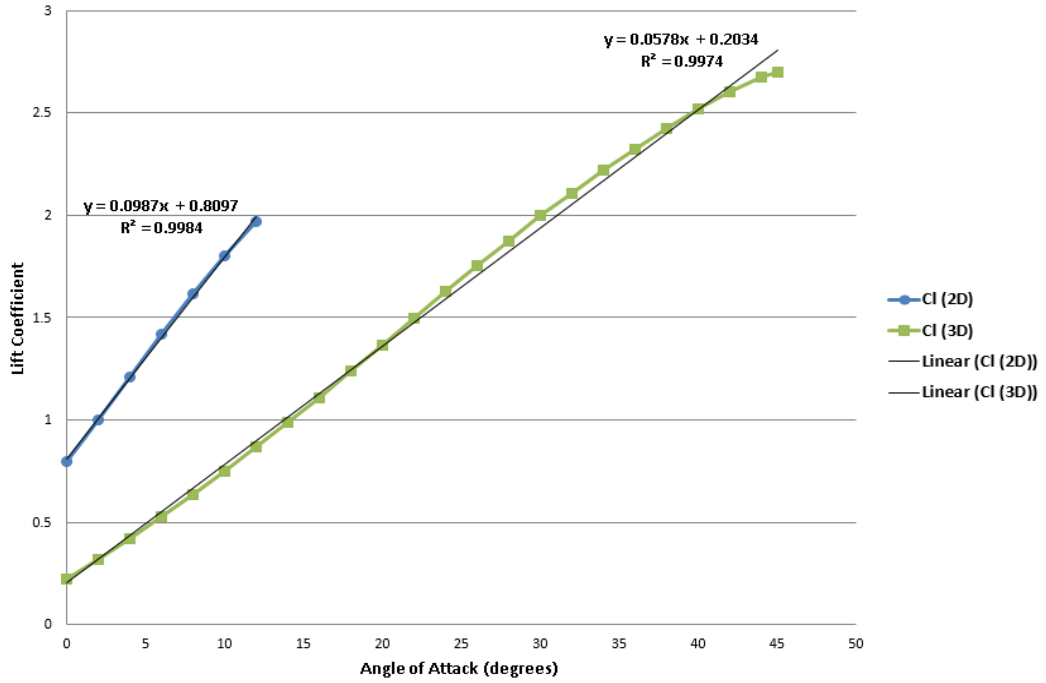

Figure 14: Comparison of 2D airfoil and 3D wingsuit lift coefficients vs. geometric angle of attack with linear curve fits

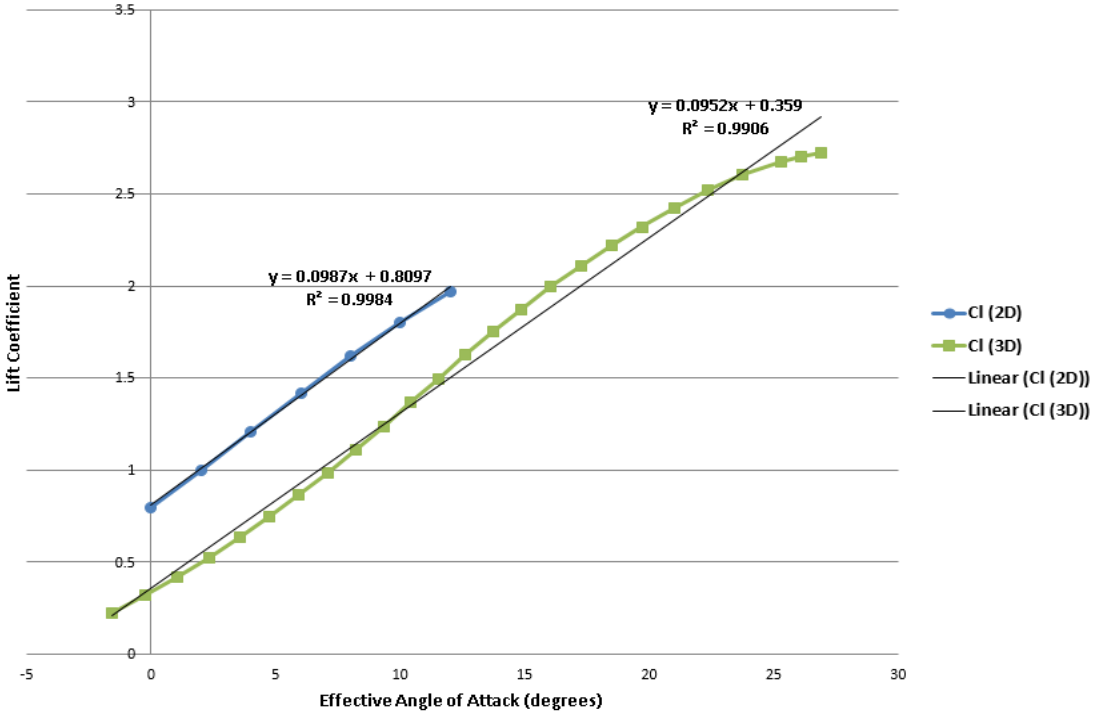

Figure 15: Comparison of 2D airfoil and 3D wingsuit lift coefficients vs. effective angle of attack with linear curve fits

The discrepancy between the predicted slope a and that obtained by CFD can be partially explained by the phenomenon of the effective angle of attack. In fact, although the induced angle of attack given by Equation (3) assumes an elliptic wing and is therefore highly approximate, it indicates that the effective angle of attack is smaller than the geometric angle of attack. The effective angle of stall is thus between 27 and 32° rather than 47°. The induced angle of attack is large because of the low aspect ratio of the wingsuit, and would be even larger if it could be calculated without the elliptic planform assumption. Plotting the 3D CFD results against the effective angle of attack rather than the geometric angle of attack brings the slope much closer to the expected value, with a value of 0.0964 as shown in Figure 15. Again, this result comes about from a big assumption as stated above. The values may not be quite accurate, but it is encouraging that the data shifts in the correct direction and comes closer to the expected values.

5.4 Rectangular Flat Plate Validation

Although a rectangular flat plate generates no lift at zero degrees angle of attack and generally generates much less lift than a wing with an airfoil cross-section, it is still useful in evaluating the general trends in the aerodynamic coefficients observed in wings of similar aspect ratios at similar Reynolds numbers. The data for rectangular plates comes from Shields and Mohseni [14]. Their data only reached a Reynolds number of the order of 10^5 rather than that of the wingsuit of 10^6, but the comparison is still worthwhile and shows a similarity that is encouraging, seen in Figure 16.

The addition of trendlines as in Figure 17 shows that the wingsuit curve has a 25% higher slope than the rectangular plate with aspect ratio 1, and a 30% higher slope than the plate with aspect ratio 1.5. Since the wingsuit has the cross-section of a cambered airfoil, it is expected to generate lift at zero degrees angle of attack, and to generate more lift than a wing without an airfoil cross-section. This trend is shown in Figure 16 and Figure 17. The higher slope is also consistent with the greater lift generated by the wingsuit in contrast to that generated by the rectangular flat plates.

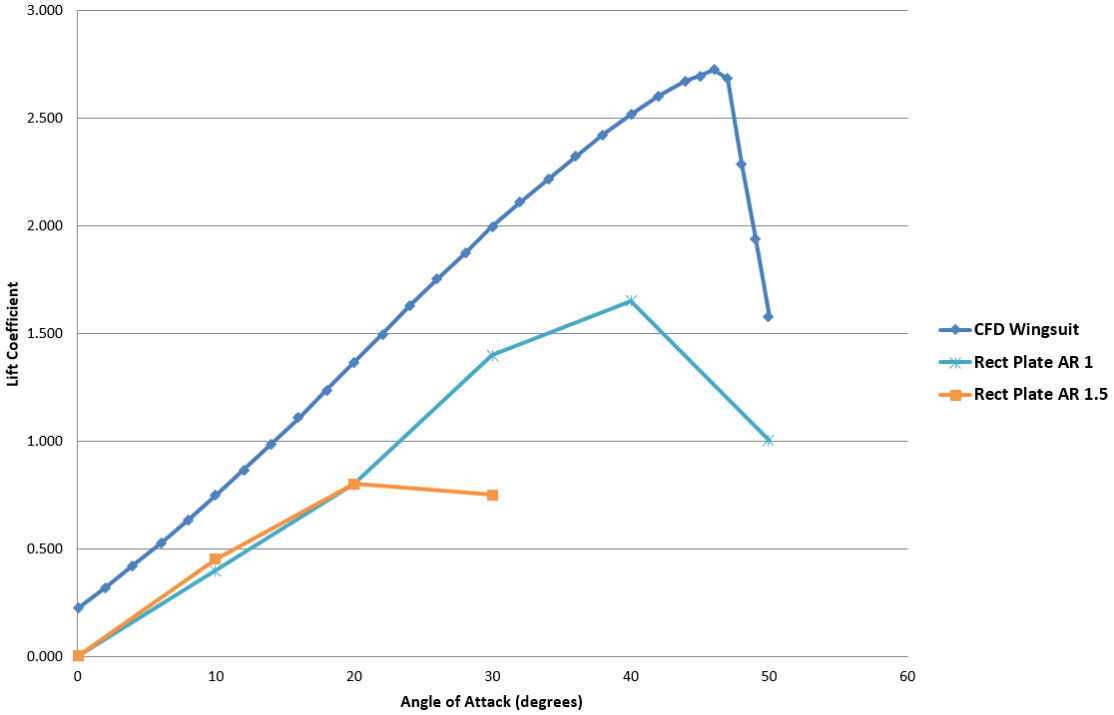

Figure 17: A comparison of lift coefficient vs. angle of attack curves for a wingsuit of aspect ratio 1.3 and rectangular flat plates of aspect ratio 1 and 1.5

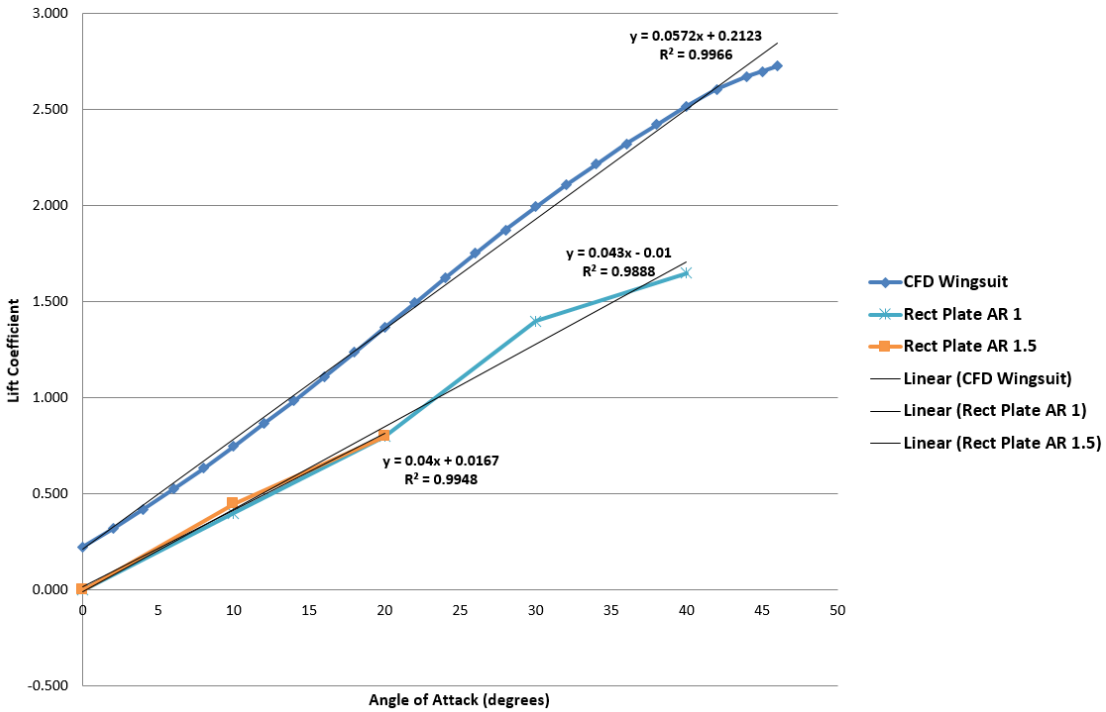

Figure 16: A comparison of lift coefficient vs. angle of attack curves for a wingsuit of aspect ratio 1.3 and rectangular flat plates of aspect ratio 1 and 1.5, with trendlines

5.5 Pressure Coefficient Plots

Knowing more about the airflow as the angle of attack increases is useful in understanding how the wingsuit would behave in actual flight conditions. Since lift is the integral of pressure, the variation of the pressure distribution around the geometry can be compared to the behavior of the lift coefficient with angle of attack. The pressure plots for four 2D cross-sections of the wingsuit were generated with the sectional views shown in Figure 18.

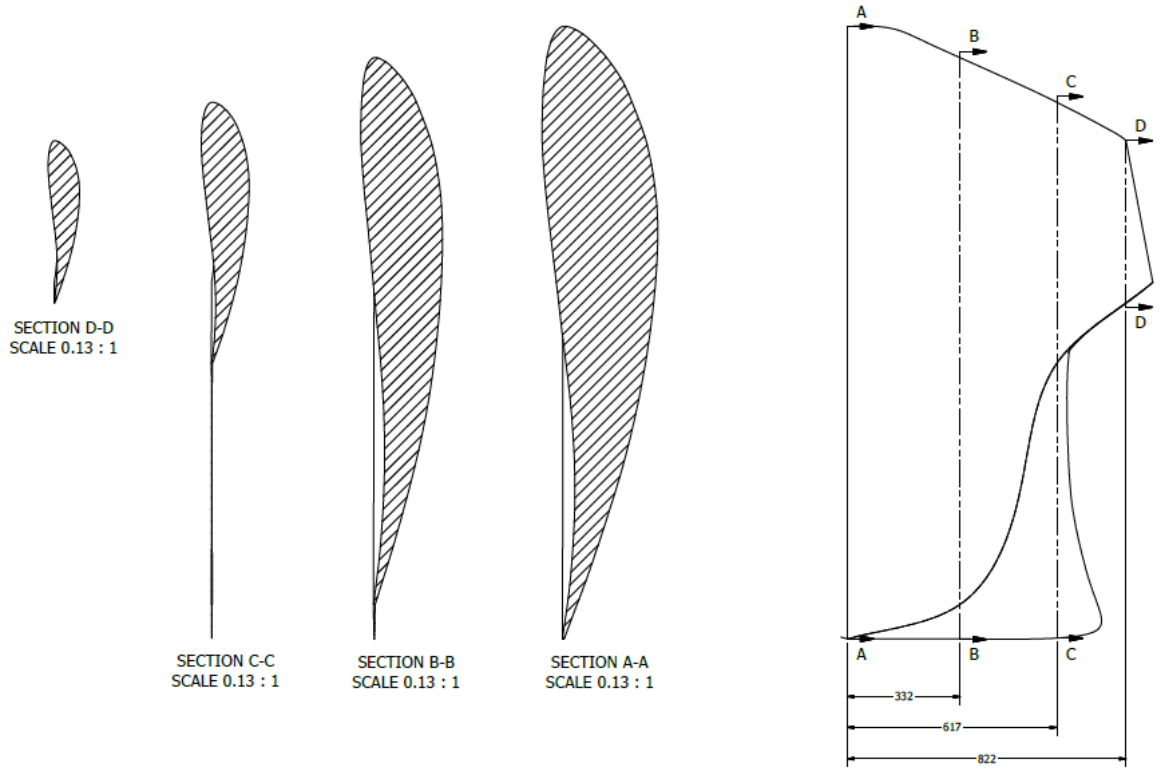

Figure 18: 2D cross-sections and locations A through D at z = 0.000, 0.332, 0.617, and 0.822 m from the center line

The pressure plots are given in Figure 19–Figure 22. For each cross-section, the pressure coefficient is plotted for 24, 32, 40, and 48° angle of attack. Each of the plots with the exception of Figure 19 shows the expected trend, in which lift increases with angle of attack. This is evident in the increase in pressure below the x-axis (i.e., under the wing) pushing the wing up as angle of attack increases. Above the x-axis (above the wing), the suction peak at the leading edge also increases with angle of attack, but decreases again after stall (48°). In Figure 19, the suction peak increases even after stall, but this anomaly could be caused by the complexity of the flow in front of the airfoil.

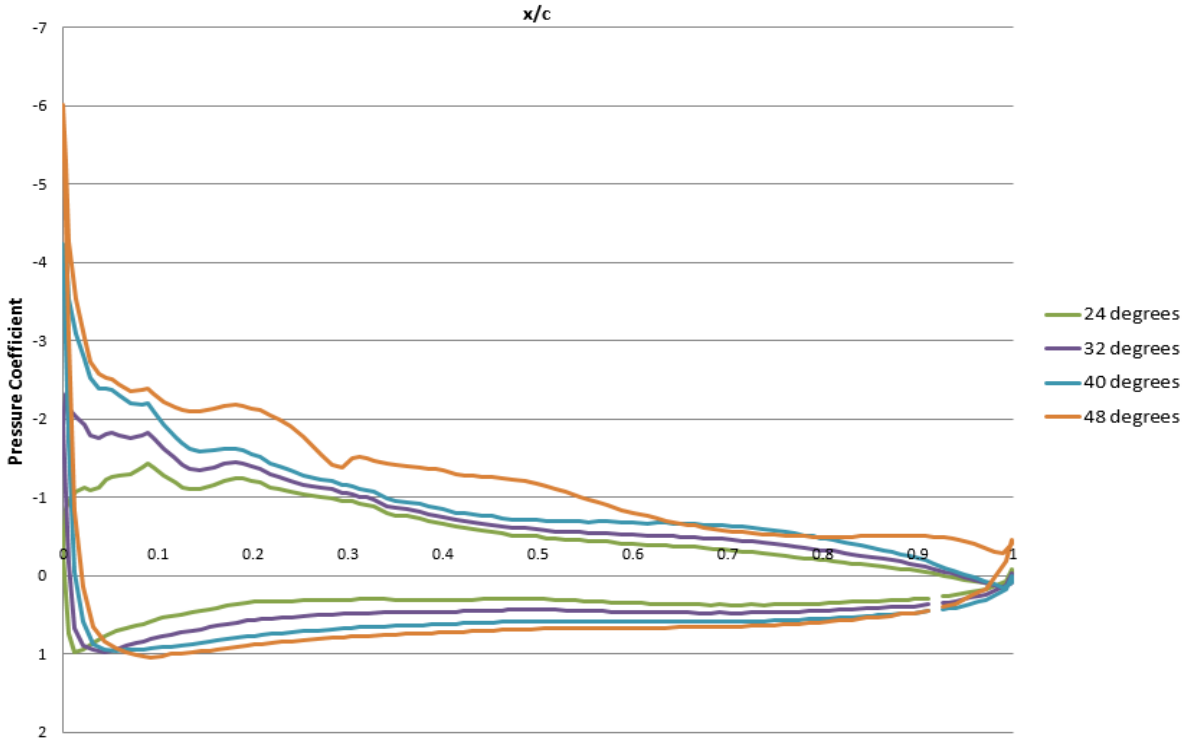

Figure 19: Pressure coefficient vs. x/c for 24, 32, 40, and 48° angle of attack at z = 0.000 m from the centerline

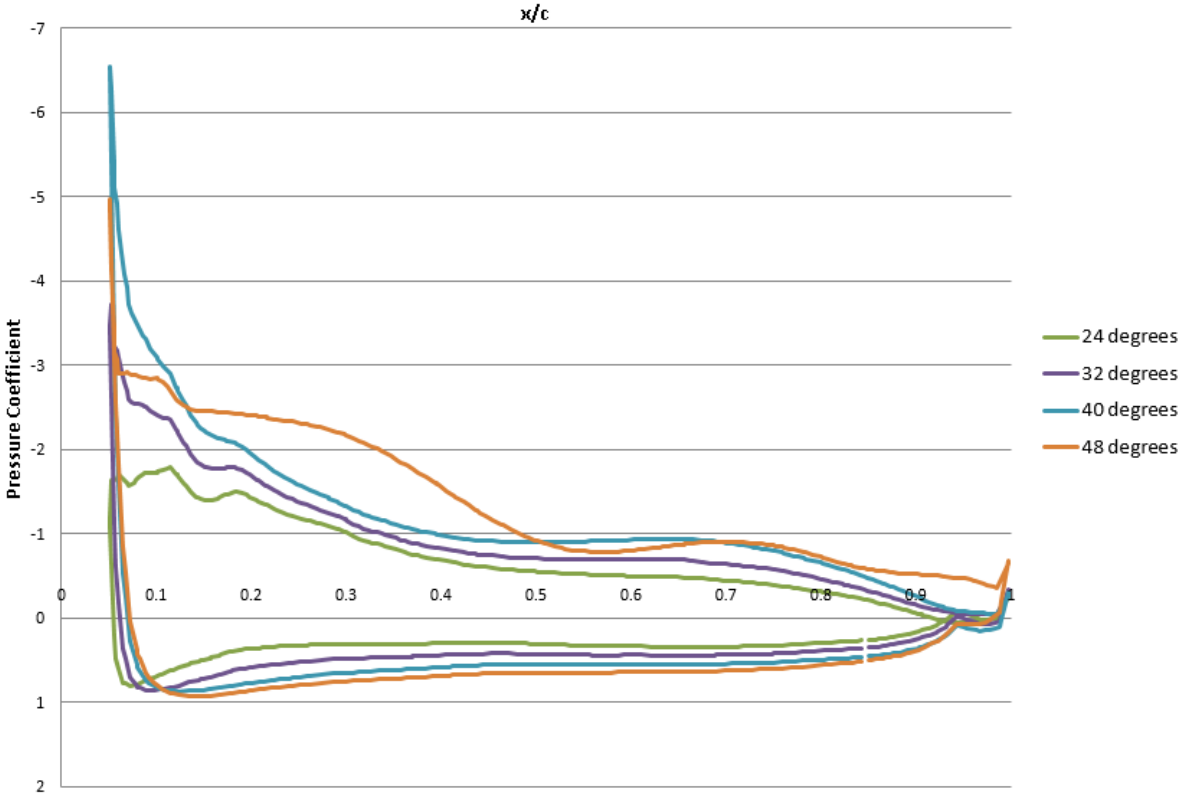

Figure 20: Pressure coefficient vs. x/c for 24, 32, 40, and 48° angle of attack at z = 0.332 m from the centerline

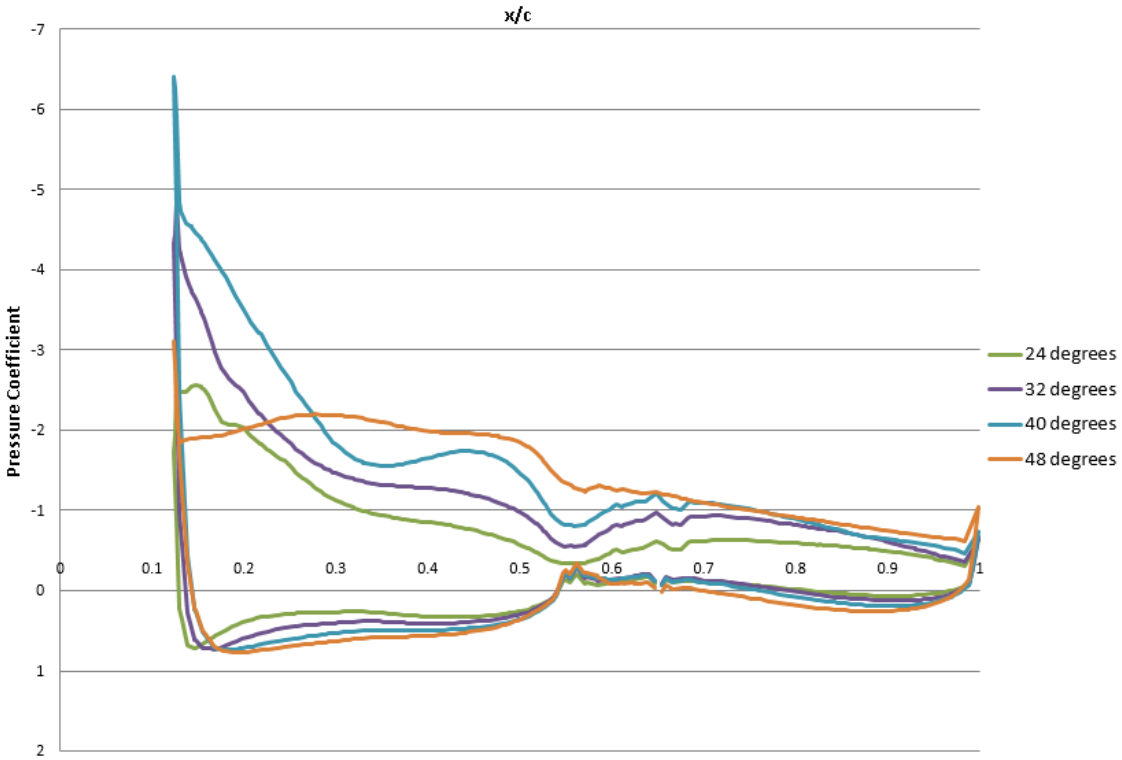

Figure 21: Pressure coefficient vs. x/c for 24, 32, 40, and 48° angle of attack at $z = 0.617$ m from the centerline

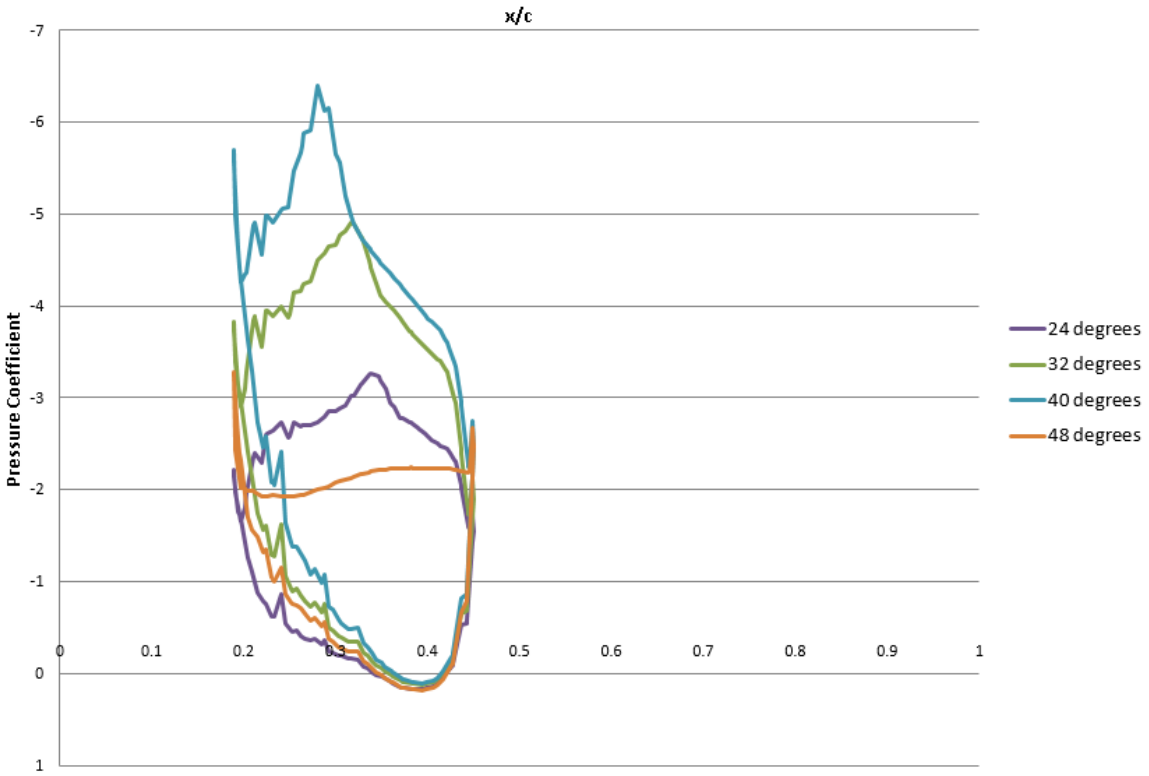

Figure 22: Pressure coefficient vs. x/c for 24, 32, 40, and 48° angle of attack at $z = 0.822$ m from the centerline

5.6 Velocity Streamlines

Velocity streamlines can be generated in 2D or 3D from a 2D or 3D surface. For this study, it was deemed most useful to generate 2D and 3D streamlines from various 2D cross-sections of the wingsuit along the x and z axes. Images of the 3D streamlines across the 3D geometry were also generated.

5.6.1 2D Velocity Streamlines from 2D Cross-Sections in z-direction

The velocity streamlines for the airfoil cross-sections cut along the z-axis were generated from the same 2D cross-sections given in Figure 18 that were used for the pressure coefficient plots. These streamlines are given in Figure 23–Figure 27.

At lower angles of attack, as seen in Figure 23, the flow is more attached, with the streamlines running smoothly over the airfoil cross-section. There is already some separation visible in the vortices shown in the other cross-sections, but the flow is mainly smooth. At stall, in Figure 26, the flow begins to detach and circulate over the top of the airfoil. After stall, in Figure 27, an enormous separation bubble is clearly evident in all four cross-sections, especially at the wingsuit centerline. Since such separation bubbles are typically the cause of stall, this result is as expected.

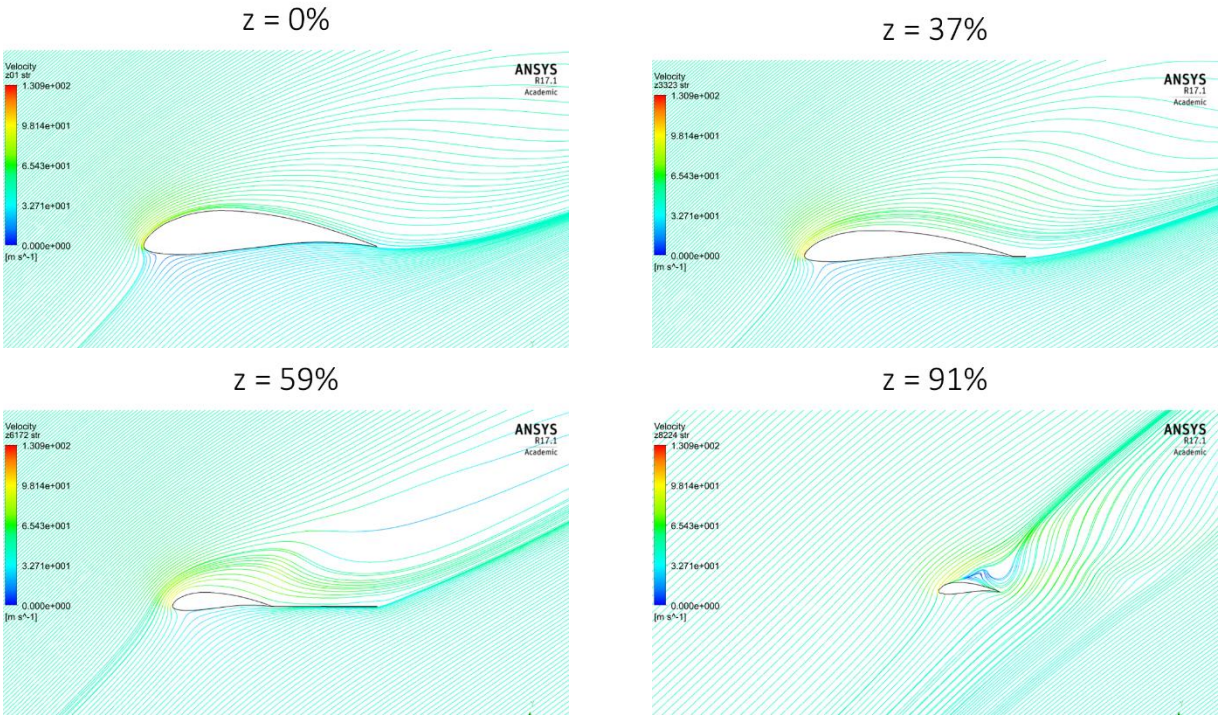

Figure 23: 2D velocity streamlines at 42° angle of attack from 2D cross-sections cut along the z-axis at 0%, 37%, 59%, and 91% from the wingsuit centerline

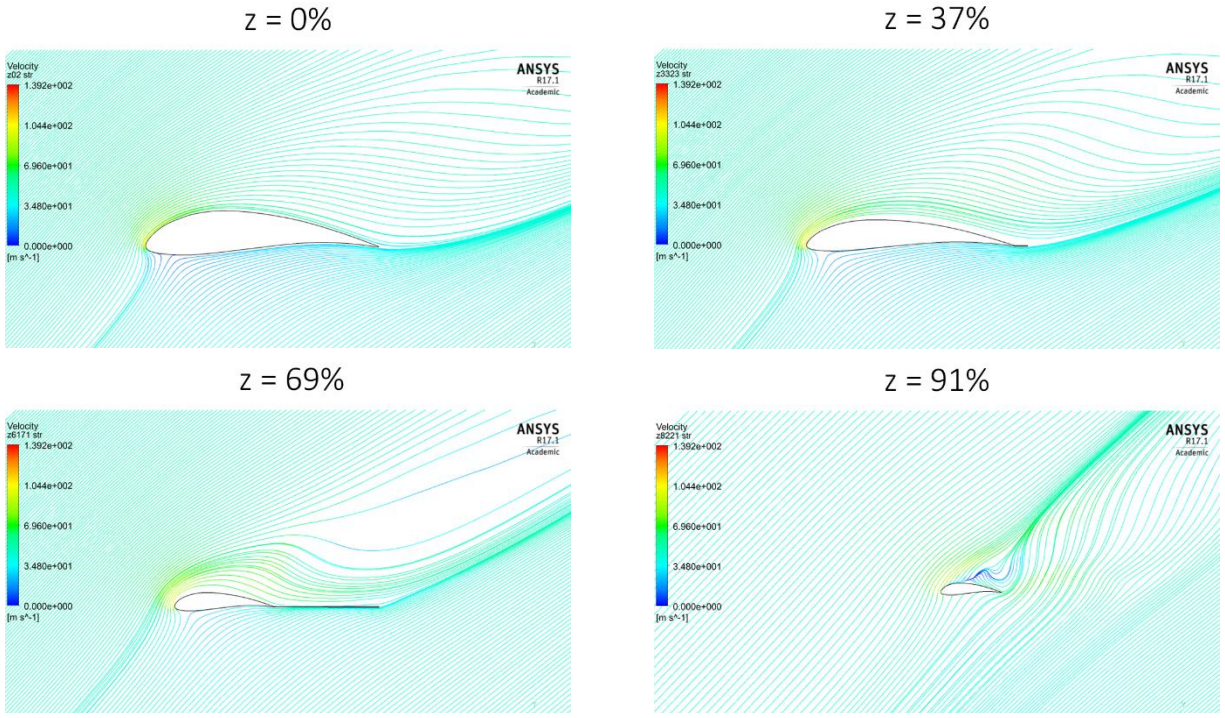

Figure 24: 2D velocity streamlines at 45° angle of attack from 2D cross-sections cut along the z-axis at 0%, 37%, 59%, and 91% from the wingsuit centerline

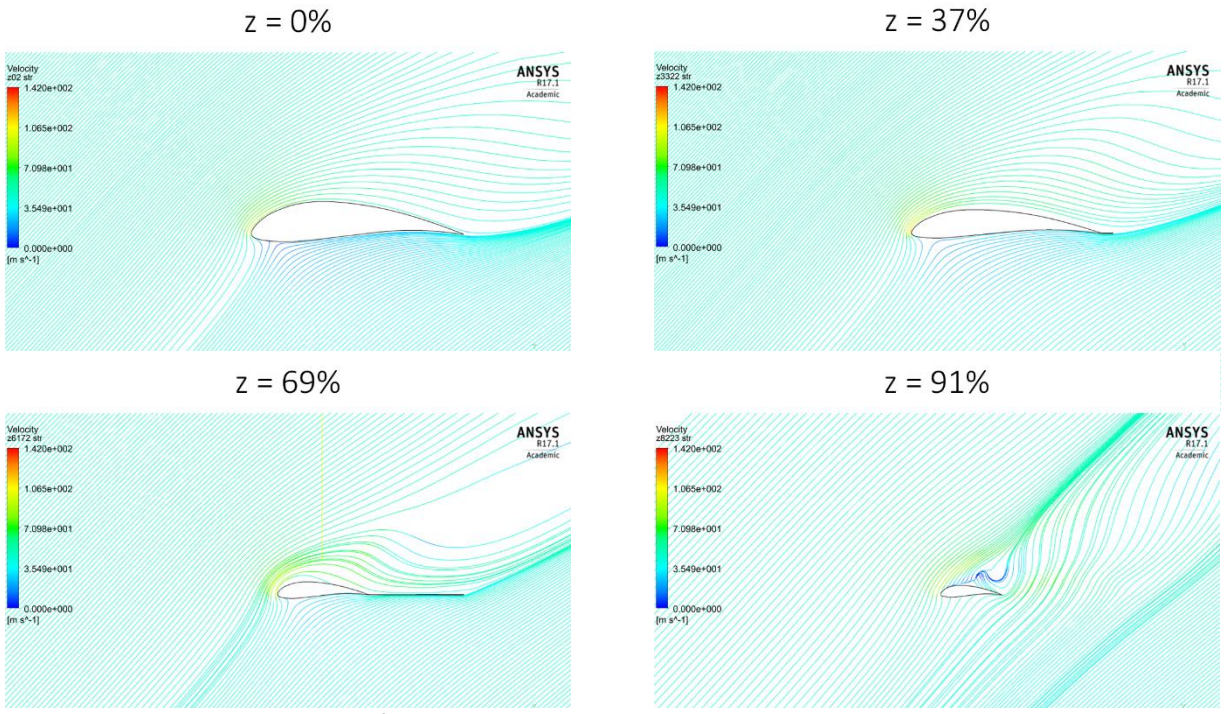

Figure 25: 2D velocity streamlines at 46° angle of attack from 2D cross-sections cut along the z-axis at 0%, 37%, 59%, and 91% from the wingsuit centerline

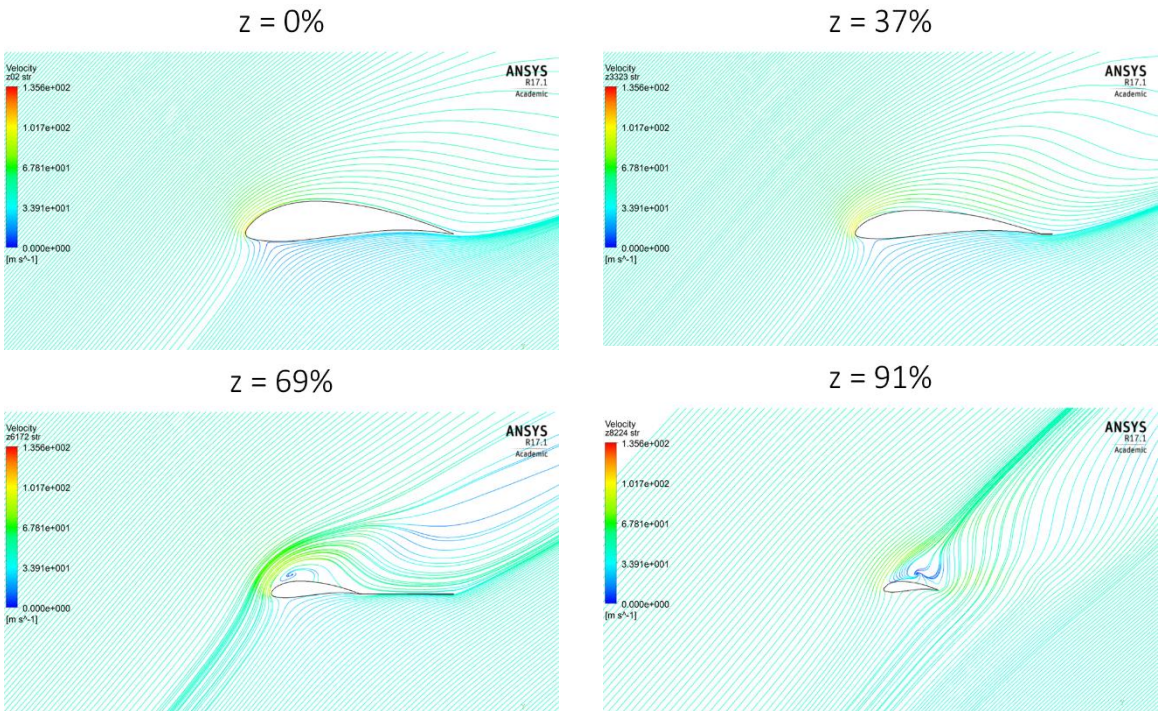

Figure 26: 2D velocity streamlines at 47° angle of attack from 2D cross-sections cut along the z-axis at 0%, 37%, 59%, and 91% from the wingsuit centerline

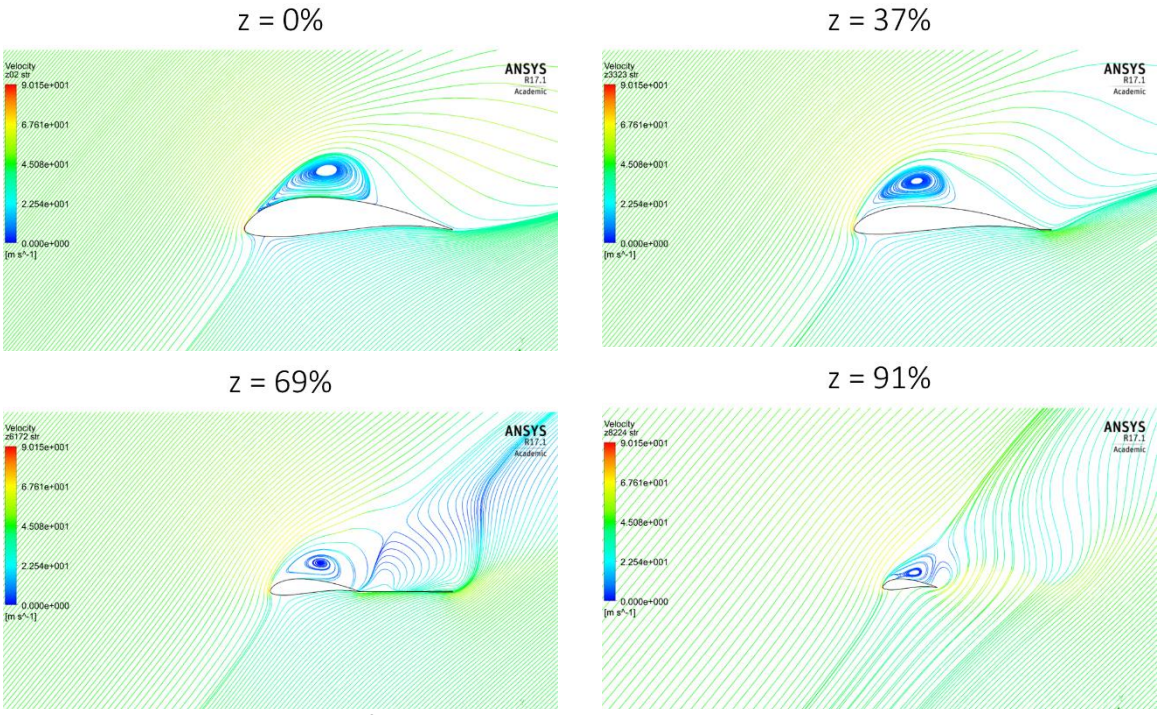

Figure 27: 2D velocity streamlines at 49° angle of attack from 2D cross-sections cut along the z-axis at 0%, 37%, 59%, and 91% from the wingsuit centerline

5.6.2 3D Velocity Streamlines from 2D Cross-Sections in z-direction

The same trends observed in the 2D velocity streamlines in Figure 23–Figure 27 can also be observed in the 3D velocity streamlines coming from the same 2D cross-section. In 3D, the wingtip vortices are easily visible and increase in turbulence and decrease in concentration with angle of attack. The trends in the wingtip vortices are consistent with the results of Shields and Mohseni [14]: the tip vortices produce crossflow that reaches more of the wing due to its low aspect ratio, creating the nonlinear increase in lift at higher angles of attack, and the wingtip vortices detach after stall, which causes a decrease in induced drag and therefore a decrease in the drag coefficient [14]. Evidence of the detachment of the wingtip vortices is visible in the lack of concentration in the vortices in Figure 32 and Figure 38.

The images of the 3D streamlines for 2D airfoil cross-sections cut along the z-axis are given in Figure 28–Figure 32.

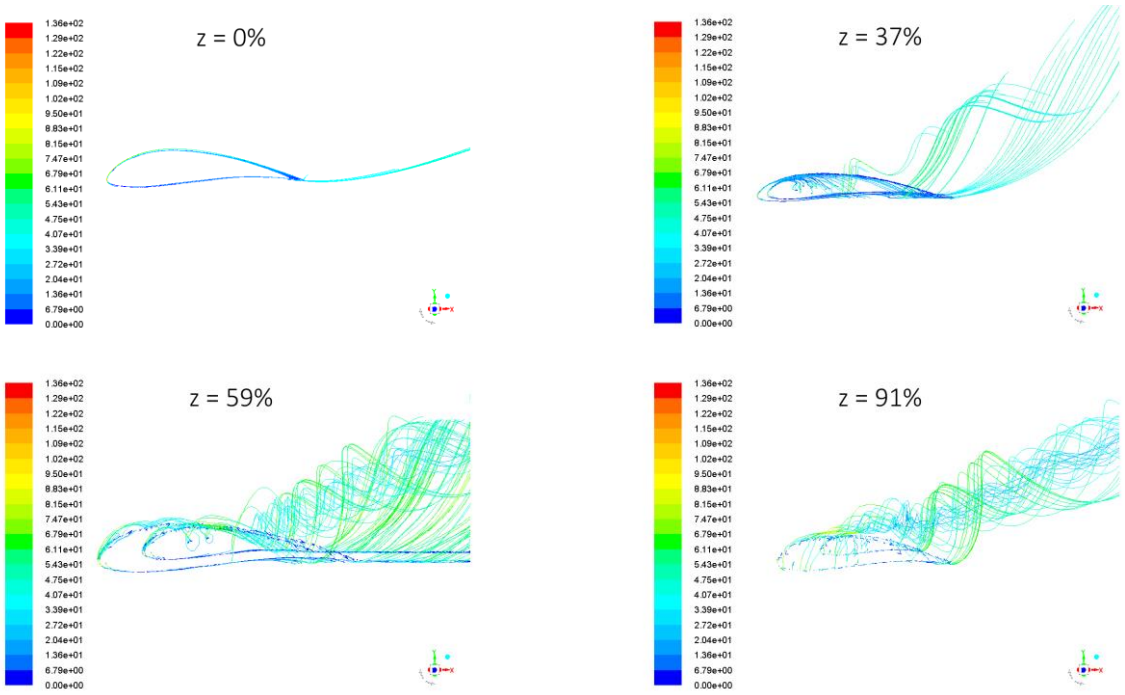

Figure 28: 3D velocity streamlines at 42° angle of attack from 2D cross-sections cut along the z-axis at 0%, 37%, 59%, and 91% from the wingsuit centerline

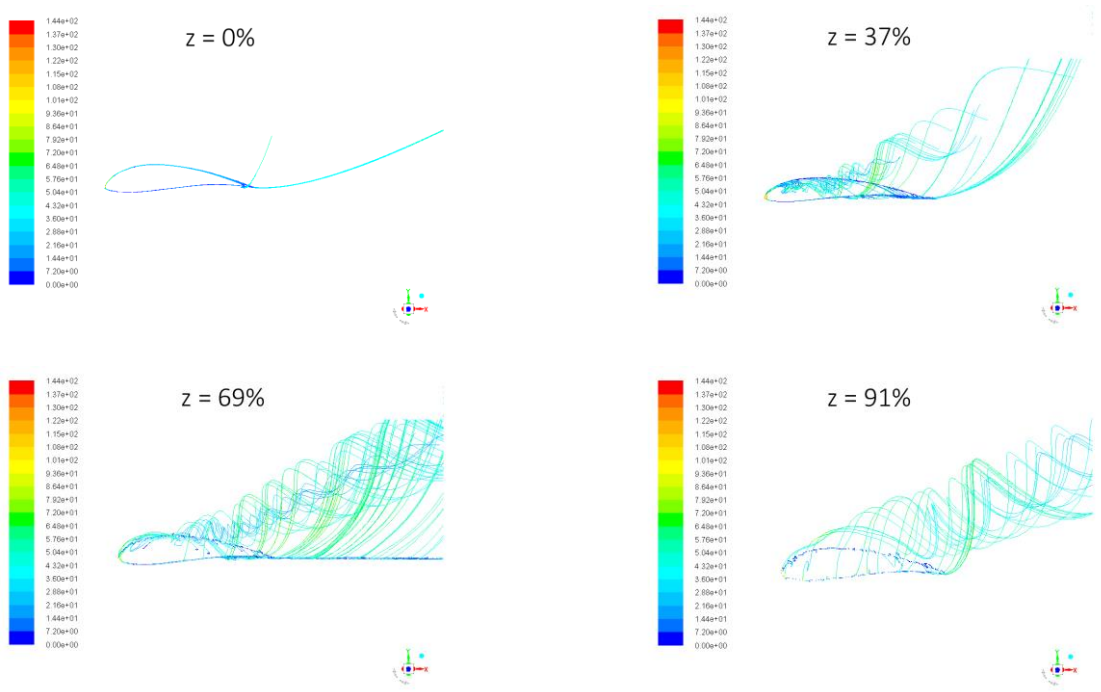

Figure 29: 3D velocity streamlines at 45° angle of attack from 2D cross-sections cut along the z-axis at 0%, 37%, 59%, and 91% from the wingsuit centerline

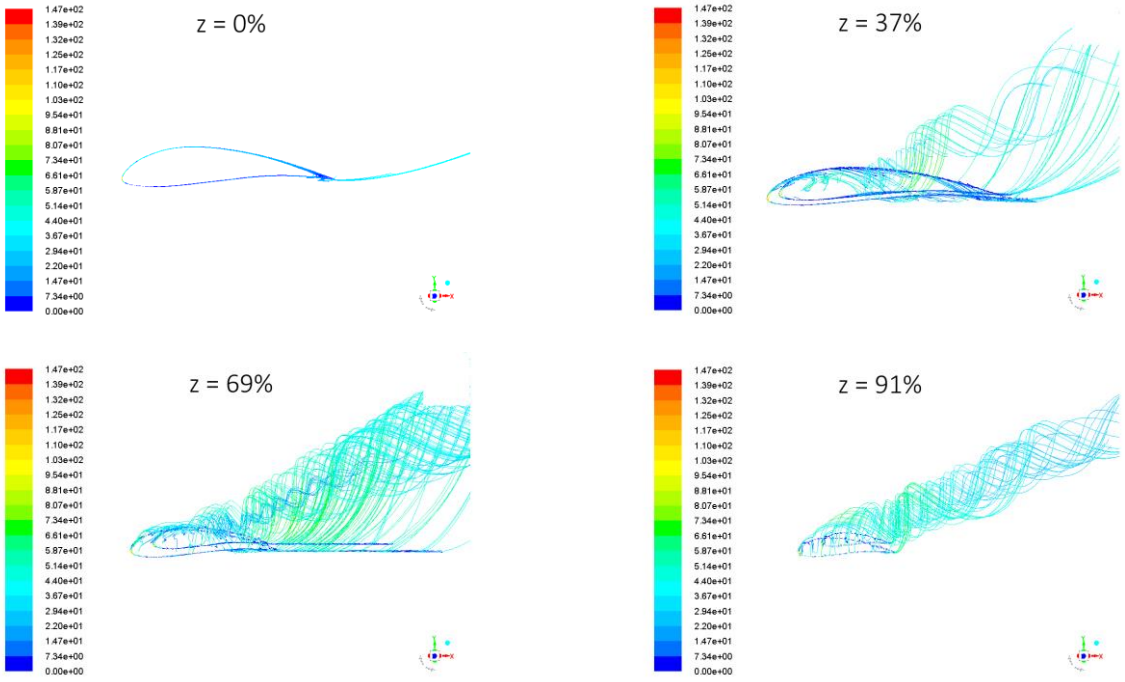

Figure 30: 3D velocity streamlines at 46° angle of attack from 2D cross-sections cut along the z-axis at 0%, 37%, 59%, and 91% from the wingsuit centerline

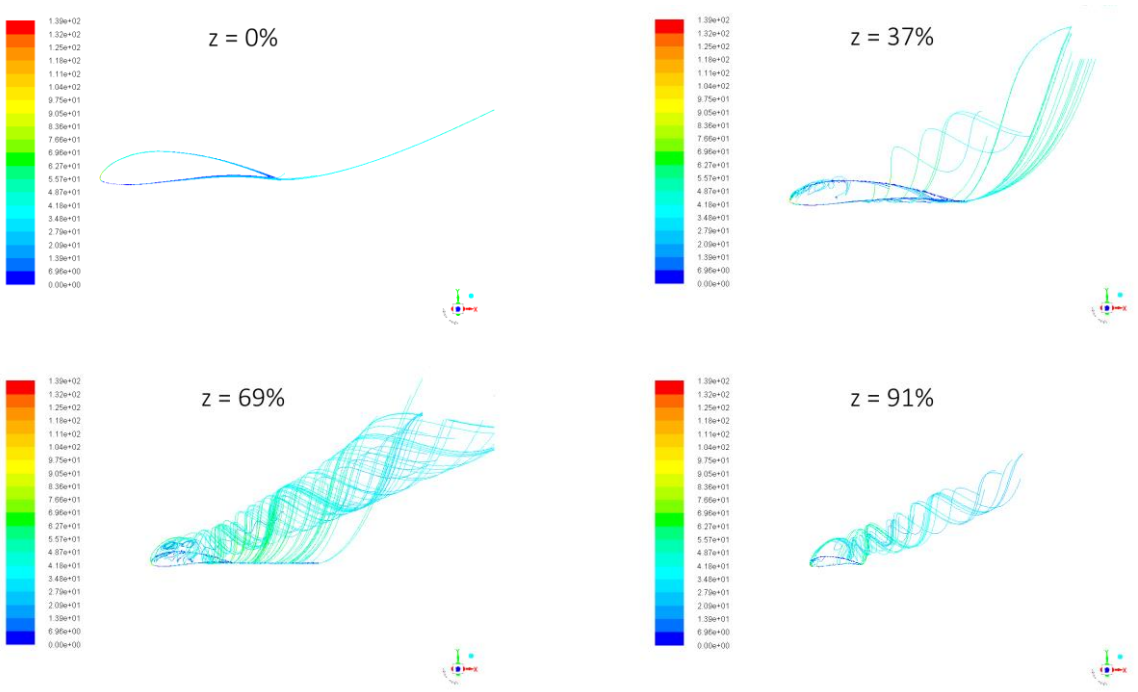

Figure 31: 3D velocity streamlines at 47° angle of attack from 2D cross-sections cut along the z-axis at 0%, 37%, 59%, and 91% from the wingsuit centerline

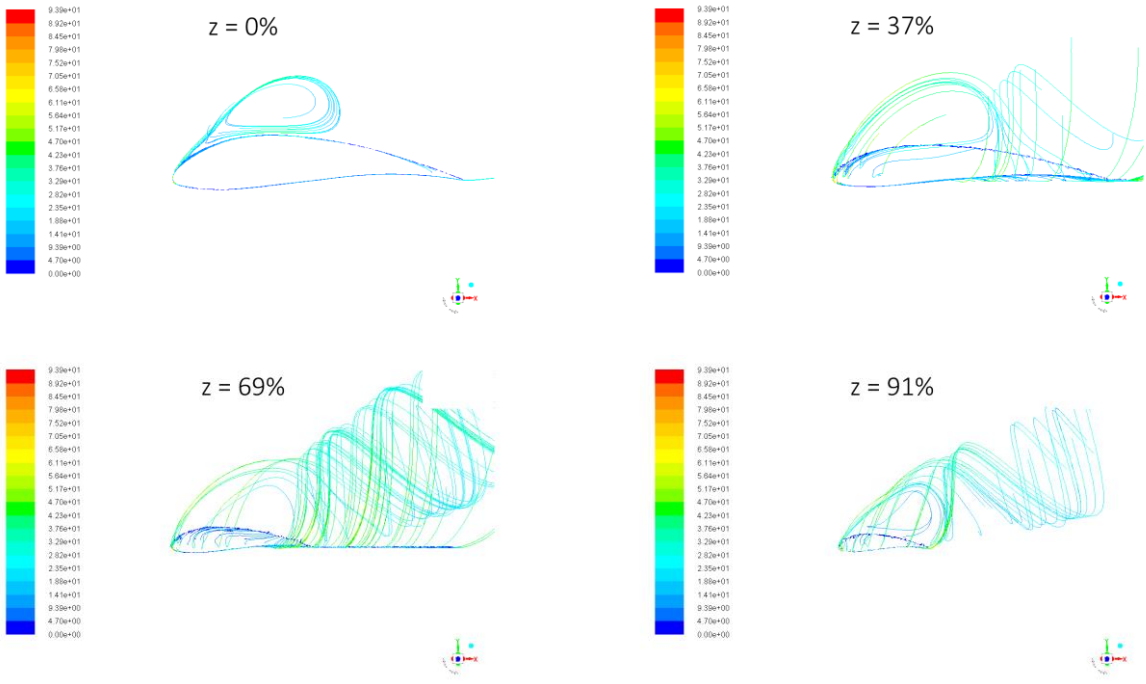

Figure 32: 3D velocity streamlines at 49° angle of attack from 2D cross-sections cut along the z-axis at 0%, 37%, 59%, and 91% from the wingsuit centerline

5.6.3 3D Velocity Streamlines from 2D Cross-Sections in x-direction

Though slightly less useful than the airfoil cross-sections along the z-axis, the 2D cross-sections produced from cutting along the x-axis also show interesting trends as angle of attack increases. The cross-sections used are shown in Figure 33 and the streamline plots are given in Figure 34–Figure 38. At lower angles of attack, the wingtip vortices are concentrated. As the wingsuit approaches stall in Figure 37, the vortices grow in size and are more diffused. After stall in Figure 38, there is no concentration of the wingtip vortices. These trends are consistent with the behavior of the aerodynamic force coefficient curves as described by Shields and Mohseni [14].

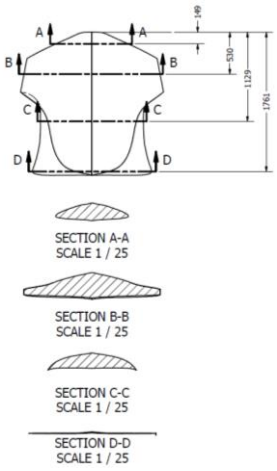

Figure 33: 2D cross-sections and locations A through D at x = 0.149, 0.530, 1.13, and 1.76 m from front of wingsuit

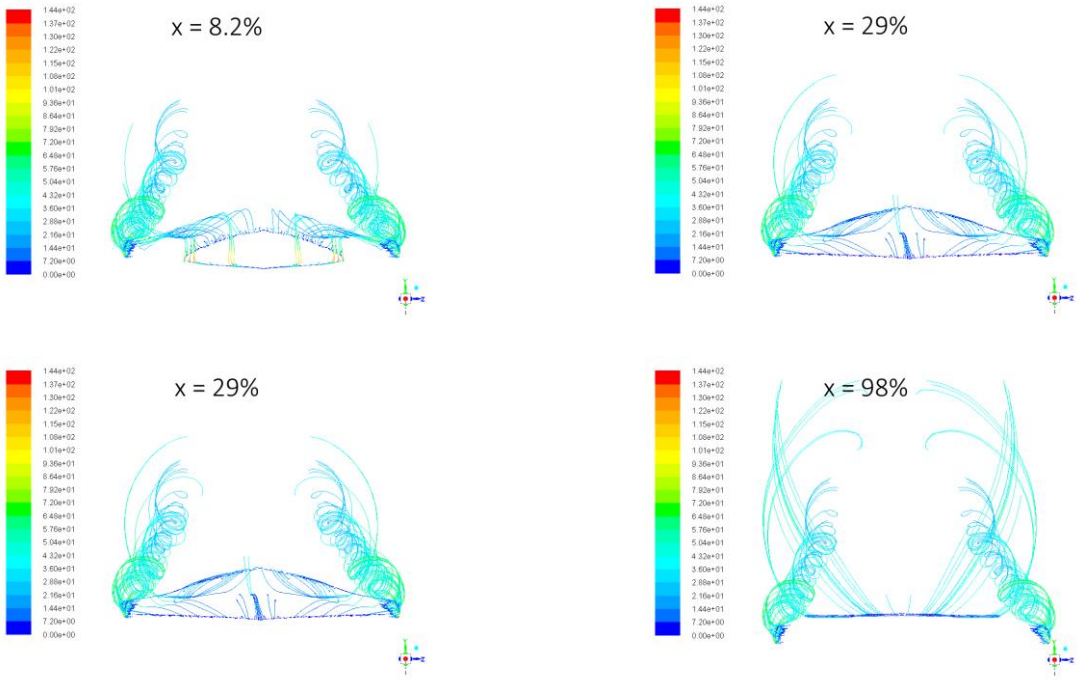

Figure 34: 3D velocity streamlines at 42° angle of attack from 2D cross-sections cut along the x-axis at 8.2%, 29%, 63%, and 98% from the front of the wingsuit

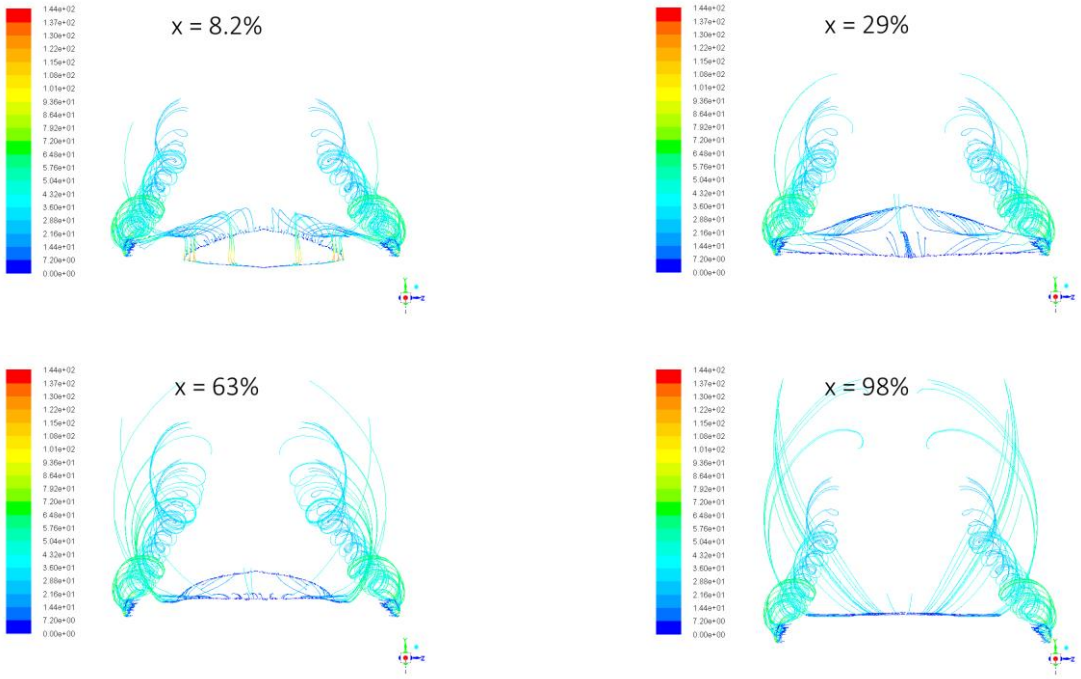

Figure 36: 3D velocity streamlines at 45° angle of attack from 2D cross-sections cut along the x-axis at 8.2%, 29%, 63%, and 98% from the front of the wingsuit

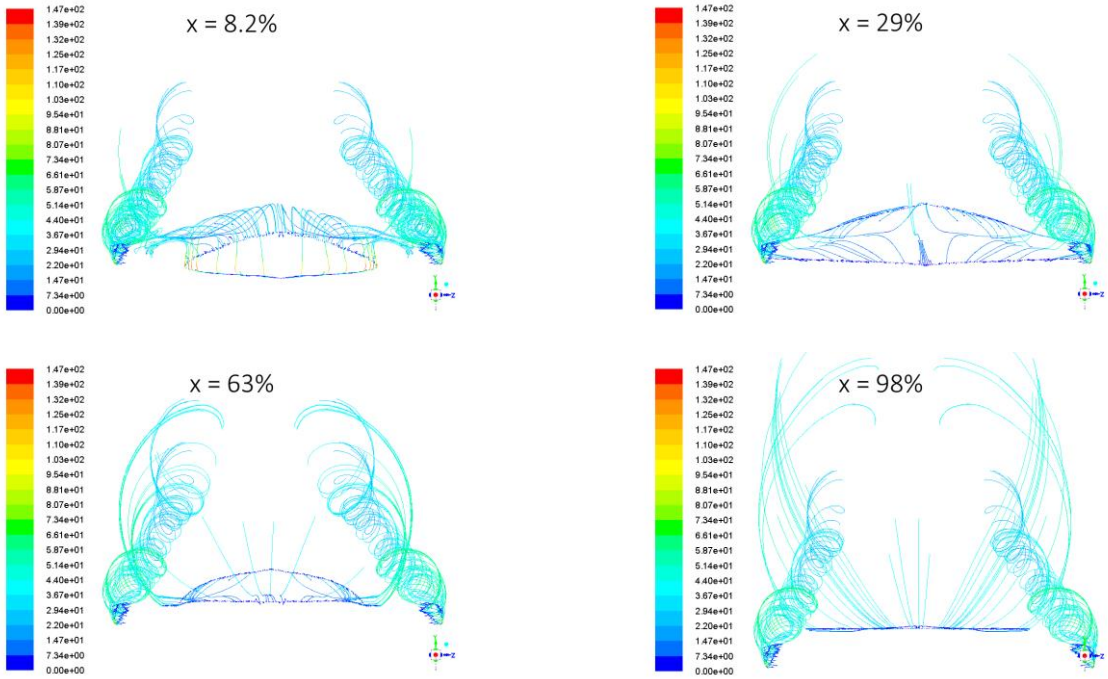

Figure 35: 3D velocity streamlines at 46° angle of attack from 2D cross-sections cut along the x-axis at 8.2%, 29%, 63%, and 98% from the front of the wingsuit

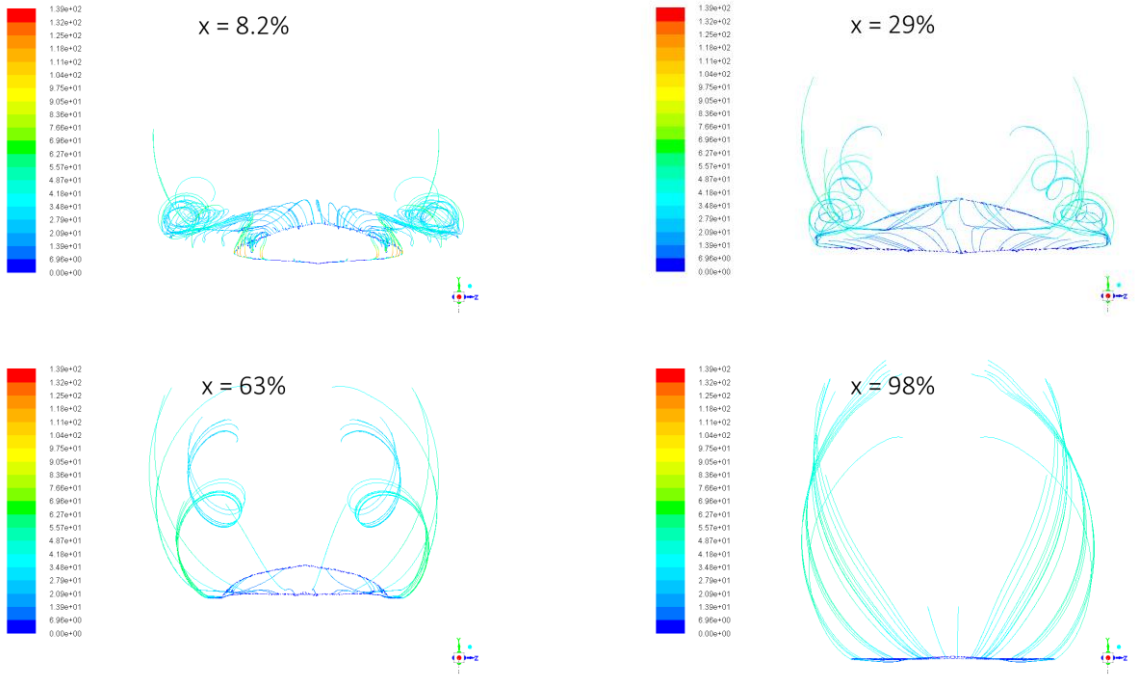

Figure 37: 3D velocity streamlines at 47° angle of attack from 2D cross-sections cut along the x-axis at 8.2%, 29%, 63%, and 98% from the front of the wingsuit

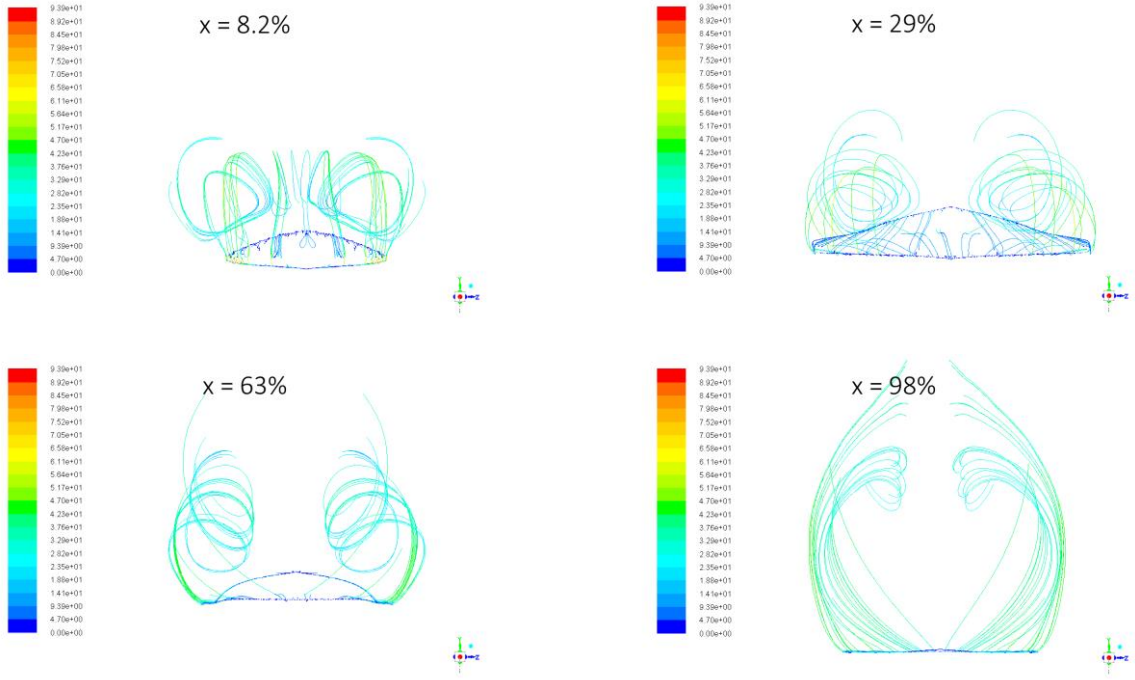

Figure 38: 3D velocity streamlines at 49° angle of attack from 2D cross-sections cut along the x-axis at 8.2%, 29%, 63%, and 98% from the front of the wingsuit

5.6.4 3D Velocity Streamlines from the 3D Wingsuit Model

Finally, the flow can also be visualized in 3D. Figure 39 and Figure 40 show the velocity streamlines across the wingsuit at 12° and 32° angle of attack, respectively. The streamlines are colored by the modified turbulent viscosity and demonstrate the increase in size and turbulence in the wingtip vortices as the angle of attack increases.

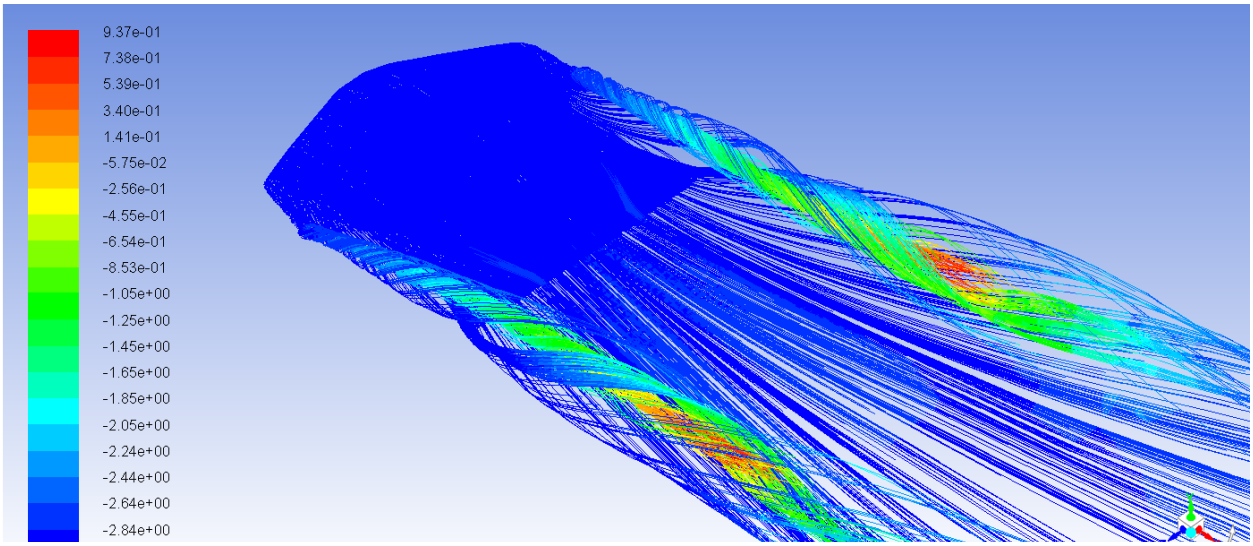

Figure 39: 3D velocity streamlines at 12° angle of attack from 3D wingsuit geometry

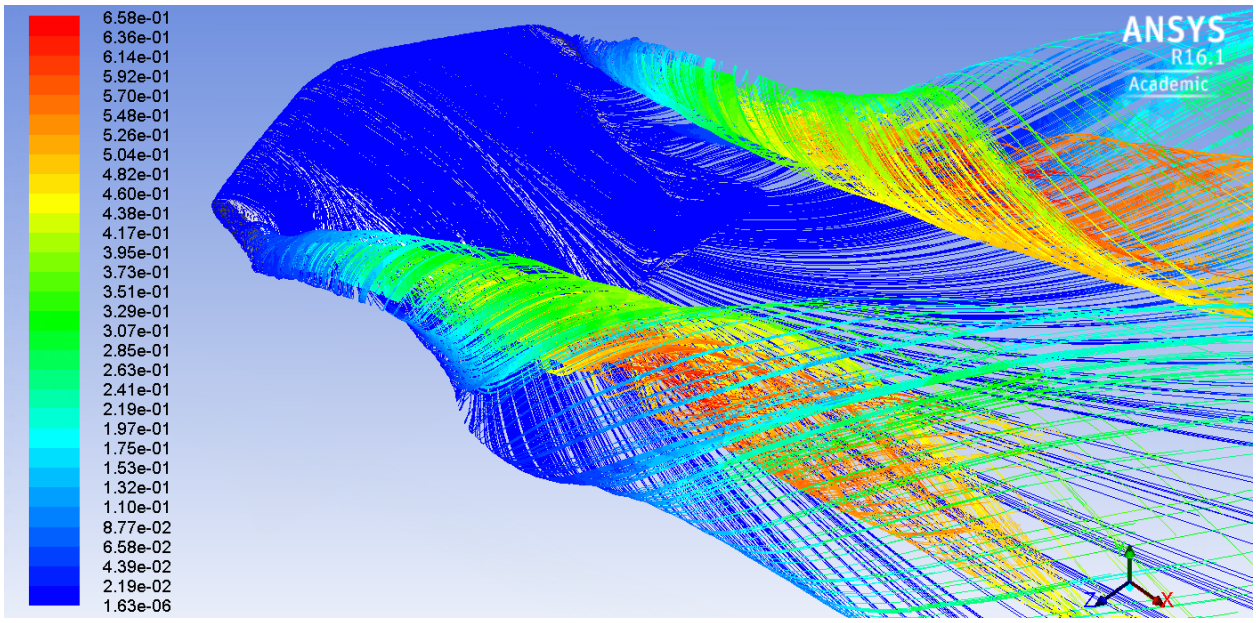

Figure 40: 3D velocity streamlines at 32° angle of attack from 3D wingsuit geometry

Chapter 6 Stability Analysis

6.1 Center of Gravity

For use in the stability analysis, the center of gravity of a human wearing the wingsuit was calculated. The center of gravity of a person was used rather than the center of gravity of the wingsuit geometry since the wingsuit itself has very little mass, and most of the weight distribution would be determined by the body of the human wearing the suit.

The typical center of gravity of a human male is 57% of his height, and that of a female is 55% of her height, measured from the feet up [16]. Since the wingsuit geometry did not include the head, the head height must be subtracted from the overall calculations. For men and women in the 99th percentile, the average head height is 23.9 cm. In the 50th percentile, it is 21.8 cm [17]. The range in the potential center of gravity was created by assuming a male with a tall (99th percentile) head or a female with a shorter (50th percentile) head.

The calculation was performed using the following methodology for a male with a head height in the 99th percentile, and a similar one for a female with a head height in the 50th percentile, with variables defined in Figure 41:

$$L = 0.57h$$

$$K = h - L$$

$$n = k - m$$

$$p = h - m$$

$$\bar{x}_{CG} = n/p$$

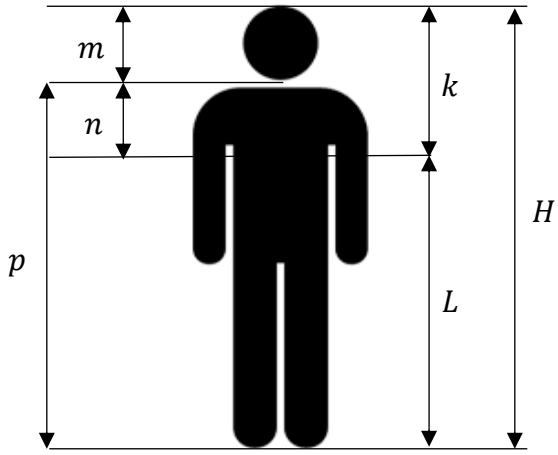

Figure 41: Geometry for center of gravity calculations for a human body

The calculations yielded a center of gravity ratio $\bar{x}_{CG}$ of 0.343 for a male with a tall head, and an $\bar{x}_{CG}$ of 0.375 for a female with a shorter head. Unlike the center of gravity ratios found in literature, which are measured from the feet up, these values are measured from the leading edge of the wingsuit.

6.2 2D Airfoil Stability

As explained previously in Section 1.2.3, it is required that the aerodynamic center is behind the center of gravity. The aerodynamic center of an airfoil is located at the quarter chord point [9], and since the airfoil cross-section is the wingsuit cross-section, its center of gravity can be considered to be at the same location. Thus, the center of gravity is at 0.343 or 0.375. The aerodynamic center of the 2D cross-section is 0.25, which is in front of the center of gravity—an unstable result. However, unlike the 2D case with a constant aerodynamic center, the 3D case has a variable aerodynamic center and can still be stable for a certain range of angles of attack.

6.3 3D Wingsuit Stability

Both the small angle approximation of Equation (6) and the full expression in Equation (5) from Section 1.2.3 were used to solve for $\bar{x}_{AC}$ for each set of angles of attack. The position of the aerodynamic center was then compared to the center of gravity. With the origin at the leading edge of the wingsuit, this means that the position of the aerodynamic center should be at a greater distance from the origin than the position of the center of gravity. The relative positions of the aerodynamic center and center of gravity can be seen in Figure 42. Thus, the region under the light blue dotted line can be considered unstable, the region between the two lines can be unstable or stable depending on the physiology of the flyer, and the region above the dark blue dotted line can be considered stable. Assuming large angles, this results in a stable region beginning at 13° angle of attack for the minimum $\bar{x}_{CG}$ and a stable region beginning at 23° angle of attack for the maximum $\bar{x}_{CG}$. The sharp changes in the aerodynamic center for higher angles of attack mean that this data should not be trusted; it is likely that after 30° or 40° angle of attack the wingsuit would become unstable due to flow separation or other factors not related to the position of the aerodynamic center and center of gravity.

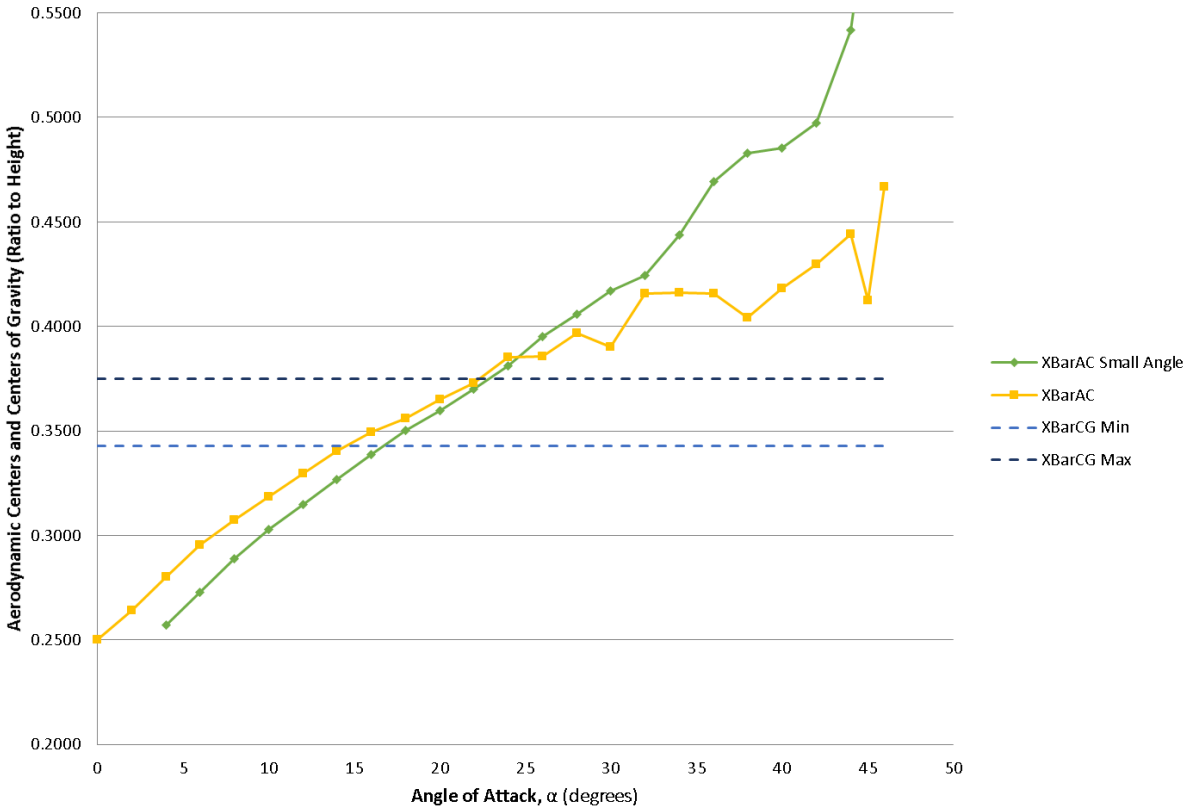

Figure 42: Position of the aerodynamic center using the small angle approximation (6) and using the full equation (5) and position of center of gravity vs. angle of attack, given as ratio of distance from the front of the wingsuit to total wingsuit height

Chapter 7 Conclusions and Future Research

7.1 Conclusions

A major obstacle to wingsuit research and development is the lack of information available, but each research project lays groundwork for the next. This study used the lack of information on wingsuit geometry as an opportunity to examine the behavior of an ideal wingsuit with an appropriate airfoil cross-section.

In this study, the 2D GOE 228 airfoil cross-section is chosen and the flow field computations are validated against the airfoil data in Profili 2.0. The lift and drag coefficient curves produced by the CFD software ANSYS Fluent with the k-kl-ω Transition turbulence model match the Profili curves very well, with a maximum lift coefficient of 1.97 and an angle of stall of 12°.

The 3D wingsuit has a maximum lift coefficient of 2.73 and a stall angle of 47°. The lift curve increases linearly until the angle of attack approaches stall, and the drag curve increases until it experiences a sharp drop near the stall angle. These results are consistent with the aerodynamics of a low aspect ratio, low Reynolds number wing [14].

The comparison of the 3D wingsuit results to the 2D airfoil results showed that the general trends in the lift curve followed the approximate predictions from wing theory. The lift curve compared well to the results for rectangular flat plate wings of aspect ratio 1 and 1.5. The pressure coefficient plots supported the results for the lift coefficient, showing the same changes in lift with angle of attack. The velocity streamlines showed separation at and after stall as expected, and the behavior of the wingtip vortices was consistent with the expected aerodynamic behavior.

The wingsuit was found to be statically stable for 18–23° angles of attack and higher. The designed wingsuit should perform well aerodynamically under typical wingsuit flying conditions. Although the results at this stage may not be directly applicable to the creation of a wingsuit, the methodology laid out in this study paves the way for other designers to follow its example in the design of commercial wingsuits.

7.2 Future Research

Although the validation techniques for the 3D case seem to indicate that the results of the 3D simulations are reasonable, the computed values should be compared to an experimental data set for true validation. It might also be worthwhile to run the same cases with different turbulence models to gain more confidence in the simulation results. Future work might include more realistic geometries that take into account human features. Some studies have successfully used laser scanners to create 3D dynamic models [12], an approach that provides a high level of accuracy and detail. A fluctuating geometry that simulates the motion of the flexible wingsuit fabric could also be considered.

References

[1] M. Abrams, Birdmen Batmen, and Skyflyers: Wingsuits and the Pioneers who flew in them, fell in them, and perfected them, New York: Harmony Books, 2006.

[2] R. Lamb, "How Wingsuit Flying Works," HowStuffWorks, [Online]. Available: http://adventure.howstuffworks.com/wingsuit-flying.htm. [Accessed 3 March 2015].

[3] W. S. Weed, "The Flight of the Bird Men," Popular Science, 18 June 2003. [Online]. Available: http://www.popsci.com/military-aviation-space/article/2003-06/flight-bird-men. [Accessed 20 April 2015].

[4] Birdman International, "Birdman Story," Birdman International, [Online]. Available: http://www.bird-man.com/company/story/. [Accessed April 2015].

[5] C. Hoffman, "Jump. Fly. Land.," Air & Space Smithsonian, November 2010. [Online]. Available: http://www.airspacemag.com/ist/?next=/flight-today/jump-fly-land-57152778/. [Accessed March 2015].

[6] R. D'Andrea and G. Robson, "Longitudinal Stability Analysis of a Jet-Powered Wingsuit," *AIAA Journal,* 2010.

[7] F. M. White, Viscous Fluid Flow, New York, NY: McGraw-Hill Education, 2005.

[8] "Improved Wingsuit Design," Discovery Communications, 23 November 2009. [Online]. Available: https://www.youtube.com/watch?v=ThXwCXV_olM. [Accessed 22 April 2015].

[9] J. D. Anderson, Fundamentals of Aerodynamics, New York, NY: McGraw Hill, 2011.

[10] K. Nyberg, "Flow Analysis of Apache Wingsuit," FS Dynamics, Stockholm, Sweden, 2012.

[11] M. Berry, J. Las Fargeas and K. Blair, "Wind Tunnel Testing of a Novel Wingsuit Design," *International Sports Engineering Association,* 2010.

[12] B. Read, "Falling with Style," Royal Aeronaurical Society, 20 September 2016. [Online]. Available: https://www.aerosociety.com/news/falling-with-style/. [Accessed 27 March 2017].

[13] G. Torres and T. Mueller, "Low-Aspect Ratio Wing Aerodynamics at Low Reynolds Numbers," *AIAA Journal,* vol. 42, pp. 865-873, 2004.

[14] M. Shields and K. Mohseni, "Effects of Sideslip on the Aerodynamics of Low-Aspect Ratio Low-Reynolds-Number Wings," *AIAA Journal,* vol. 50, no. 1, 2012.

[15] ANSYS, Inc., ANSYS Fluent Theory Guide, Canonsburg, PA: ANSYS, Inc., 2013.

[16] N. W. W. L. K. Hamilton, "Chapter 14: Center of Gravity and Stability," in *Scientific Basis of Human Motion*, 11 ed., Boston, MA, McGraw-Hill Higher Education, 2008.

[17] Wikipedia, "Head Anthropometry," [Online]. Available: https://upload.wikimedia.org/wikipedia/commons/6/61/HeadAnthropometry.JPG. [Accessed 23 3 2017].

[18] Wikipedia, "The Flying Taylor," [Online]. Available: https://upload.wikimedia.org/wikipedia/commons/d/d5/Flying_tailor.png. [Accessed 24 March 2017].

[19] "The Birdman," [Online]. Available: http://the.birdman.free.fr/a-bird-pic02.htm. [Accessed 24 March 2017].

Vita

Maria E. Ferguson

Degrees

M.S. Aerospace Engineering

Department of Mechanical Engineering and Materials Science,

Washington University in St. Louis, May 2017

B.S. Mechanical Engineering

Department of Mechanical Engineering and Materials Science,

Washington University in St. Louis, May 2016

B.A. 3+2 Engineering

3+2 Engineering Program,

Saint Mary's College of California, May 2016